Approach to Qualification for Electron Beam Powder Bed Fusion in Ti-6Al-4V

A Thesis Presented for the
Master of Science
Degree
The University of Tennessee, Knoxville

Sean Lucas Yoder
December 2018

Copyright © 2018 by Sean L. Yoder
All rights reserved.

ACKNOWLEDGEMENTS

I would like to thank Dr. Suresh Babu, Dr. Ryan Dehoff, Dr. Peeyush Nandwana, Dr. Vincent Paquit, Dr. Michael Kirka, Chase Joslin, Larry Lowe, James Ferguson, Jessie McPeters, Dr. Fatmata Barrie, Derek Morin, and staff from Arcam AB for allowing me the opportunity to work with them and help advance research at the MDF.

I am especially thankful for my parents, Jim and Denise Yoder, and other family, friends, and supporting individuals who helped me through this journey. I would like to personally thank my supporting wife, Lindsey Yoder, and my dog, Sadie, for keeping me grounded during this adventure.

ABSTRACT

Recent developments in additive manufacturing (AM) show promise for using AM manufactured components in a production setting. However, a crucial step for mass producing AM components is to certify these parts for use. One common method for certifying parts is to manufacture tensile coupons alongside any parts. These coupons are characterized and the results are related to the parts. This causes many researchers to focus on the process-material interactions while neglecting build setup. Another issue related to certification of AM parts is the lack of knowledge in the software calculations for a given process. Original equipment manufacturers (OEM), such as Arcam AB for electron beam powder bed fusion (E-PBF), need secrecy in their software to ensure their scan strategy is protected. Therefore, this practice provides researchers little information or confidence about changes made in process parameters. To provide insight into these areas of variation, the current work can be broken into two parts – (i) understanding how changes in selected process parameters can influence non-selected parameters and (ii) determining the effectiveness of current qualification methods for the E-PBF process.

To better understand process parameters, changes in selected process parameters were simulated and compared with the Arcam provided parameter set. Results of these simulations show that speed function variable is only a function of melting time while modifications to the contour passes and surface temperature result in changes to the heat balance. Variations in the heat balance change the cooling rate of as-fabricated material, which causes microstructural evolution in titanium alloys. Preliminary results show that modifying the surface temperature for specific regions can be used to control microstructure.

To better understand how build setup can influence parts in a build, build setup variables such as part melt order, build volume, and cross-sectional melt area were modified between two builds. Results of these changes show that performance in test coupons cannot be applied to performance in the other parts since changes in build setup influence each part differently. The current work provide challenges to applying traditional qualification methods to AM fabricated components in hopes that a process-based certification path can be achieved.

TABLE OF CONTENTS

Chapter One Introduction 1
Chapter Two Background & Literature Review 3
Understanding Arcam AB Q-Series 3
General Machine & Build Setup 3
Design Guidelines Related to Build Setup 7
Data Collection 8
Microstructural Characteristics of Ti-6Al-4V 14
Fundamentals of Ti-6Al-4V 14
Phase Transformation of Ti-6Al-4V 19
Process Parameter Relationships 20
Mechanical Behavior of Ti-6Al-4V 21
Relevance to Current Work 23
Chapter Three Experimental Procedure 25
Experimental Setup 25
Materials Characterization 32
Polishing & Etching Techniques 32
Microstructural Imaging & Measurements 32
Tensile Testing 33
Chapter Four Results And Discussion 34
Process Parameter Mapping for Process Controlled Microstructure 34
Build Setup Variable Evaluation 42
Chapter Five Conclusions and Future Work 54
List of References 57
Appendix 61
Vita 71

LIST OF TABLES

Table 1: Software version, processing themes, and powder used for Process Parameter Mapping 27
Table 2: Set list of process parameter changes 27
Table 3: Software version, processing themes, and powder used for Process Controlled Microstructure 29
Table 4: Software version, processing themes, and powder used for Build Layout Variation 31
Table 5: α – Lath measurements of samples shown in Figure 3 & Figure 6 comparing Melt Order, Sample Location, and Build Number 44
Table 6: Mean, Standard Deviation, and Unpaired T-Test of tensile testing results comparing Ultimate Tensile Strength, Yield Strength, and Elongation between Build 1 & 2. 46

LIST OF FIGURES

Figure 1: Q-Series Machine from Arcam AB [2] 4
Figure 2: Internal hardware for the Q-series machine [2]..... 5
Figure 3: Falcon (Top) and Talon (Bottom) Interface with NIR Images 10
Figure 4: Beam Current Visualization Tool..... 11
Figure 5: EDEN Interface with Selected Key Variables 13
Figure 6: Paraview Interface with Build Layout Setup 13
Figure 7: Material properties of common materials compared to titanium [10]..... 15
Figure 8: Unit cell of α lattice (left) and β lattice (right) [10] 16
Figure 9: Effect of alloying elements on the β transus temperature [10]..... 16
Figure 10: Martensitic (left) and Massive (right) α phases at a cooling rate of 525°C/s and 20°C/s [11] 18
Figure 11: Continuous cooling diagram for Ti-6Al-4V [11] 18
Figure 12: Schematic phase diagram of Ti-6Al-4V (left) and a simplified thermal process showing phase transformation of E-PBF process (right) [13] 20
Figure 13: Effect of cooling rate from the β phase on yield strength and elongation [10]22
Figure 14: Arcam Test Artifact Layout (A) with one image of the total build cross section (B) 26
Figure 15: ORNL Test Artifact 2 Layout with Varying Cross-Sectional Melt Area from High (Red) to Low (Blue)..... 29
Figure 16: Build Layout isometric and top view (A) where yellow, green, and blue signify melt order 1, 2, & 3, respectively. (B) Side view of fixture spacing to show changes in part spacing between Build 1 and 2 31
Figure 17: Comparison of Set 1: Standard Melt Theme (Top) and Set 2: Reducing the Post Heat Time (Bottom) 36
Figure 18: Comparison of Set 1: Standard Melt Theme (Top) and Set 16: Increasing Speed Function (Bottom)..... 36
Figure 19: Comparison of Set 1: Standard Melt Theme (Top) and Set 12: Removing Contours (Bottom) 38
Figure 20: Comparison of Set 1: Standard Melt Theme (Top) and Set 9: Reducing Power Temperature (Bottom) 38
Figure 21: Post Heat/Cool Time versus Temperature plot for varying surface temperature values 41
Figure 22: Comparing Samples 18 (Top) and 11 (Bottom) between the standard and modified melt themes..... 41
Figure 23: Uniaxial yield strength (MPa) results broken down by sample and x-y location on the start plate. Colors indicate melt order where yellow, green, and blue are order 1, 2, & 3, respectively. Sample labeling as follows: Build Number – Melt Order-Sample Number 43
Figure 24: X-Z micrographs of tested samples showing change in microstructure from top to middle (2-L7 & 2-L18) and similarity from middle to bottom (2-L18 & 2-F19) 43
Figure 25: Yield Strength (MPa) versus Elongation (%) of Samples Tested in Build 1 (Blue Squares) & Build 2 (Orange Triangles) 46

Figure 26: In-situ collected bottom temperature (C) for Builds 1 & 2 with total printing time in hh:mm 47
Figure 27: X-Z micrographs of tested samples from Build 1 (1-L18) to Build 2 (2-L18) 47
Figure 28: (a) NIR Pixel Intensity visual and plot of samples from B2 tracked for every layer. Green signifies parts printed in the center of the build plate with expected low yield strength while orange signifies parts printed on the edges of the build plate with expected higher yield strength. (b) Yield strength versus elongation of samples from B2 where center (green circle) and edge (orange triangle) parts from (a) 50
Figure 29: (a) NIR detected porosity in Samples 2-L7 & 2-F11 (b) Failure height measurements from samples tested in B2 50
Figure 30: Fracture surfaces of Samples 2-L7 & 2-F11 51
Figure 31: (a) Etched micrograph in X-Z plane of Untested Sample 2-L14. (b) Vickers Hardness test across etched region shown in (a) 53

CHAPTER ONE

INTRODUCTION

Additive manufacturing (AM) is gripping the manufacturing community with promises of creating stronger, lighter, and better components. The adaptation of AM technologies grows year after year due to its usefulness in rapidly prototyping and its ability to manufacture complex geometries. However, those in the community know that AM is not the solution to all manufacturing problems.

In general, AM processes use a layer by layer deposition approach based on a computer aided design (CAD) model. The software provided for each AM machine manufacturer accepts the 3D CAD model, slices it into 2D layer images, and generates a toolpath file for each and every layer. According to ASTM F2792, AM processes can be broken down into the following groups: binder jetting, direct energy deposition, material extrusion, material jetting, powder bed fusion, sheet lamination, and vat photopolymerization [1]. Of these seven independent processes, this thesis focuses on the electron beam powder bed fusion (E-PBF) process provided by the equipment manufacturer, Arcam AB ®. While advances in the AM community are making the process more reliable and repeatable, certification and qualification challenges still exist in the AM community, especially in the E-PBF process. Traditional qualification metrics recommend manufacturing test coupons alongside the fixtures of interest such that characterization of the coupons by mechanical testing or metallography can be related to back to the fixtures. This thesis outlines the potential dangers found in this qualification

procedure by determining how changes in process parameters and build setup can influence the final part quality of the fixtures and test coupons differently.

Work provided in this study is broken into two parts. Part 1 evaluates the interconnectivity of process parameters in order to provide confidence in experimental results. This analysis shows a comparison of simulated log file data with changes to selected process parameters in an ORNL developed visualization program, EDEN. This visualization process allows users to visually compare changes in the simulated data. Links found between surface temperature and the heating and cooling functions in are then used to control the microstructure of as-fabricated samples in a preliminary investigation of process-controlled microstructure.

Part 2 utilizes a commonly used qualification technique to print test coupons along with fixtures and mechanically test the coupons in uniaxial tension for two builds. By varying extrinsic variables such as part melt order, support structure density, and total build cross-sectional area outside of the recommended specifications, this experiment correlates the results of bulk mechanical testing and microstructural characterization with extrinsic variables found in the build setup. This study will include information from the study, “Approach to Qualification using E-PBF In-situ Process Monitoring in Ti-6Al-4V” by Sean Yoder that is in the publication process. This thesis highlights the importance of data analytics in the AM community and provide challenges to applying traditional qualification methods to AM fabricated components in hopes that a process-based certification path can be achieved.

CHAPTER TWO

BACKGROUND & LITERATURE REVIEW

This chapter discusses the background of the Arcam Q-series process and highlights areas researched by reviewing current literature related to the E-PBF process. First, it discusses the Q-series machine from the build setup procedure to data collection relevant for material characterization. Next, it highlights current literature in the electron beam powder bed fusion (E-PBF) process and how the scope of this work is relevant to the community. Finally, it will contain a brief overview of titanium microstructure, with emphasis on the Ti-6Al-4V alloy, and the relevant material properties from solid state phase transformation to bulk mechanical properties.

Understanding Arcam AB Q-Series

This section includes information to understand the Q-series hardware and software for a better understanding of the process. Figure 1 shows the Q-series machine in which all experiments for this study were performed. In general, the procedure for each build manufactured on the Q-series machine follows from build setup to process parameter selection to data collection. Each of these steps are outlined in the subsections to follow.

General Machine & Build Setup

The first step in creating a part using the E-PBF process is to prepare the build file. This process requires 3-D CAD models in the form of stereolithography (STL)

Figure 1: Q-Series Machine from Arcam AB [2]

files to be loaded into a software called Magics ®. Once in Magics ®, the STL files can be arranged, oriented, and manipulated in any possible way along with the generation of support structure to ensure build success. The STL files are converted into the Arcam Build File (ABF) format and taken to the machine to be manufactured. Once at the machine, the file is loaded into the software and all themes regarding material, build substrate plate, and processing themes are selected. The controlled vacuum seals the chamber and reduces pressure to a near vacuum for manufacturing.

Figure 2 shows the hardware for the Q-series machine. A rake system moves powder from the powder mounds over the build substrate plate before each layer. Once the build plate is covered with a 50µm layer of powder, the machines accelerates a focused beam of electrons to create an energy source sufficient for the preheat and melt

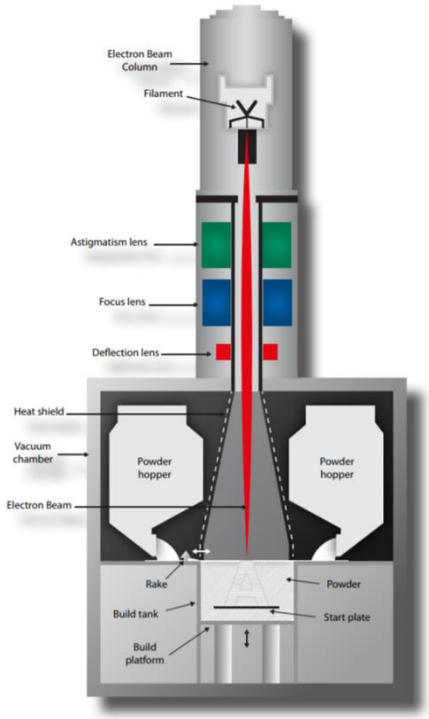

Figure 2: Internal hardware for the Q-series machine [2]

stages to occur. The focused beam is manipulated by electromagnetic pulses in the astigmatism coils to focus or dilute the energy while deflection coils maneuver the beam to the desired locations. Information about the energy and location are provided in the ABF file while the EBM control software creates a heat balance model to control the processing temperature. EBM Control utilizes the input parameters from each of the three process themes: preheat, melt, and wafer support.

The preheat theme is used to partially sinter the powder bed such that the melting stage can occur without vaporizing the powder. This theme is broken into two stages: Preheat 1 and 2. Preheat 1 defocuses the beam to a low energy density and scans over the

entire surface of the powder bed to sufficiently sinter the powder. Preheat 2 uses the same process with a higher energy density to a region offset by 4mm from the melt region. These passes create an area that the electron beam is able to move over, known as jump safe in preheat 1, and melt over, known as melt safe in preheat 2, without vaporizing the powder bed.

Next, the melting theme occurs in a linear pattern known as hatch or line melting and each hatch melt is rotated by an angle of 135 degrees every layer. Line melting is controlled by specific process parameters in the software such as current, speed, focus offset, speed function, and others where the relationship between current and speed are key for solidification of the material [3]. Other variables of interest in the melt themes include line offset spacing and focus offset which alter the raster pattern as and the shape of the melt pool [3]. Much of the proprietary algorithm developed by Arcam AB lies in this theme such that the melt optimization related to the energy balance is unknown. This can be detrimental to researchers due to the lack of confidence in their findings.

After melting, the contour pass and support structure are completed. The contour melt passes over the edges of the part to improve geometric accuracy and surface finish while the support structure provides thermal and mechanical support for the fabricated parts in processing. Finally, the machine applies a post heating stage similar to the preheat 1 stage such that the surface of the melted parts can return to the optimal temperature. The optimal temperature is set in the melt theme and applies post heat according to the energy balance equation determined by the Arcam software. This entire process is repeated for every layer until the build is completed.

Other hardware of note in the Q-series machine is the ability to use near infrared (NIR) camera, thermocouple temperature measurements, and feedback from the machine systems to generate build data. EBM Control stores process parameters, feedback readings, measured data, and build information in a process log file (plg) format. This format can be broken down into groups of data: analyze, build, OPC, process, and themes. Analyze and OPC variables are focused for the purpose of this study. Analyze data is the intent of the machine to process each layer based on the ABF file and the energy balance equation. This can be viewed as what the machine plans to do for each layer before executing that layer. Analyze functions can be generated by running a simulation of the build. The OPC variables are any data collected during the build process. This requires the machine to be processing to record feedback from hardware like the rake, vacuum pumps, high voltage. The data collection techniques and software tools used to analyze these data forms are discussed in a following subsection.

Design Guidelines Related to Build Setup

In general, designing builds for the AM processes can be challenging due to the vast number of tracked variables [4]. Variables such as part nesting, melt layer area, and support structure are constantly reevaluated to ensure build quality for both microstructure and porosity metrics. Arcam AB ® has provided a list of suggestions and rational for the E-PBF process such that quality builds can be produced faster [2]. Key takeaways relevant to this thesis are as follows.

Parts need to be oriented such that less than 30% of the melted area is changed between two layers [5]. Large changes in the melt area per layer can lead to fluctuations

in the energy input and gradients in the microstructure [6]. As the energy input fluctuates, the energy balance calculated by the software needs to compensate such that additional post-heat or post-cooling manages any energy fluctuations. This can be influential to the microstructural evolution from the variations in cooling rates, as explored in depth in the microstructure section below.

Another suggestion is to minimize the X-Y-Z footprint of the build as much as possible [5]. The main reason this is to speed up the fabrication time and limit the amount of energy needed per layer for pre- and post-heat [5]. However, changes in total build volume can influence the overall heat in the system which may also influence the cooling rate and resulting microstructure, as explored in the microstructure section below.

One last suggestion is the need for nested parts to clear 2mm from another part in order to avoid fusing them together [5]. Hrabe and Quinn found that the effect of part size on mechanical response is 1% change in ultimate tensile strength and 2% change in yield strength [7]. However, they suspect this deviation is mainly due to the change in thermal mass of nearby parts and less on the actual size of the parts. This indicates a deviation of microstructure between nested parts and those printed without that influence. Each of these suggestions provide insight into how the software handles changes in the build setup and what material properties are influenced by those changes.

Data Collection

The Q-series machine contains a near infrared (NIR) camera that collects images for every processed layer as well as feedback sensors for log file data. These images use the short wavelength infrared signal nearest to the visible light spectrum in order to detect

changes in emissivity of the surface of the powder bed. The resolution of the NIR camera on the Q10 platform allows for 100 x 100 x 50 µm voxel size. V. Paquit and his team, along with individuals at Blue Quartz, have developed Dream 3D, a characterization interface that contains filters able to process NIR images, ABF slice images, and co-register them with other useful information.

During the build process, data stored in the log file can be analyzed for each build. Typical log file structure is difficult to read and even harder to visualize; ORNL employee, Chad Steed, and his group created a program to read and visualize time series data in various ways. This allows for data analysis to become easier for both experienced and untrained eyes. Programs developed by Chad's team include Falcon, Talon, Beam Current Visualization, and EDEN.

Falcon is a multi-variant time series program that allows for visualization of log file variables from the Arcam machines. Along with visualization, simple statistical data can be determined over the build or specific layers of interest. Talon is a subprogram of Falcon, where selected data can be segmented layer by layer and visualized alongside a stack of images. Figure 3 shows the Falcon and Talon interface with typically visualized log file and near IR image data. For more information, see Chad Steed's paper titled, "Falcon: Visual Analysis of Large, Irregularly Sampled, and Multivariate Time Series Data in Additive Manufacturing" [8].

The second program developed for E-PBF technology is the beam current visualization tool. The interface, as shown in Figure 4 below, shows how each layer of the build can be broken down into colors and line segments that help to visually interpret

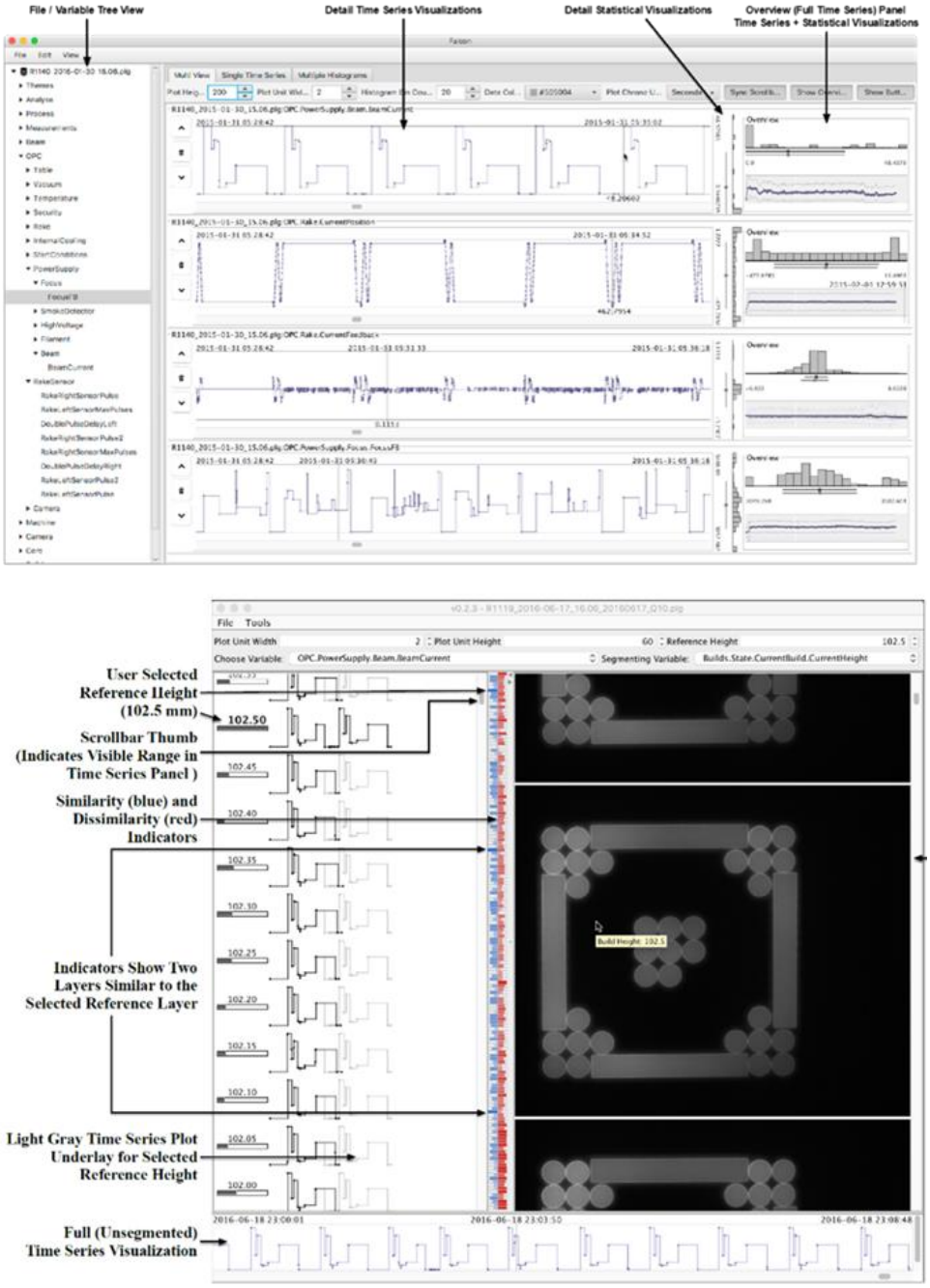

Figure 3: Falcon (Top) and Talon (Bottom) Interface with NIR Images

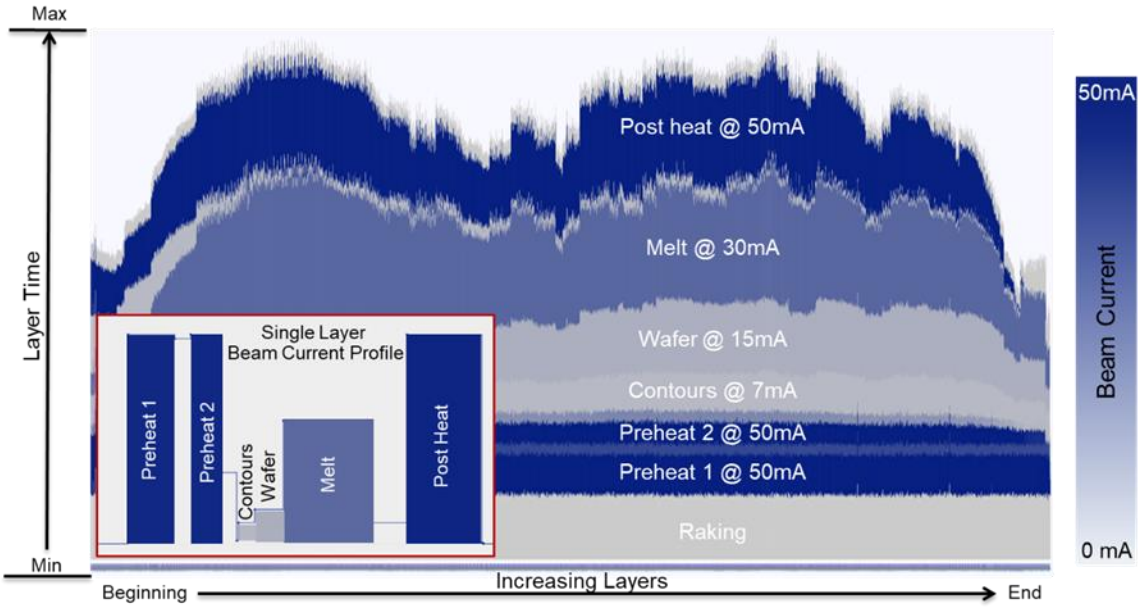

Figure 4: Beam Current Visualization Tool

beam current profiles for the entire build. Each portion of energy applied for a given layer is broken into a specific line segment and all line segments are stacked on top of one another. The length of each line segment correlates to how long each stage takes to complete. Colors ranging from grey to blue indicate the current (mA) applied for each stage of the layer. For example, both preheat stages require 50 mA of current from the beam and the build was setup such that the preheat 1 area does not change. Therefore, the first preheat line will be of consistent length and the darkest blue shade. Conversely, the melting stages varies with cross-sectional area such that the shorter lines correspond to the shorter melt time. Melting also occurs at a consistent current of 30 mA so the color is a lighter blue shade than the preheat band. A detailed diagram can be seen in Figure 4.

The Exploratory Data ENvironment (EDEN), Figure 5, is a repurposed tool developed by Chad Steed and his team to visualize trends in log file information. Each line corresponds to a string of variables that are time dependent. Thinking of a row in excel, all data found in that row will act as a line segment that is connected through each column. This allows each layer to be visualized as a line where changes in each column show up as changes between layers. EDEN has been instrumental in providing insight into the connectivity of the processing parameters. For more information, see Chad Steed's paper titled, "Big data visual analytics for exploratory earth system simulation analysis" [9]. Figures found in the results and discussions sections below will focus on the visualization of log files in the EDEN interface; however, all programs were useful in determining the changes in log file variables.

Along with log file data for each build, the Q-series machine contains a near infrared (NIR) camera that collects images for every processed layer after the melt occurs. These images have the capability to collect multiple data modalities such as pixel intensity and porosity content while storing simulation data, log file information, and more into one convenient Dream3D data set for analysis. Once the data has been processed, Paraview is used to visualize the data set. Figure 6 shows the Paraview interface with the porosity information visualized.

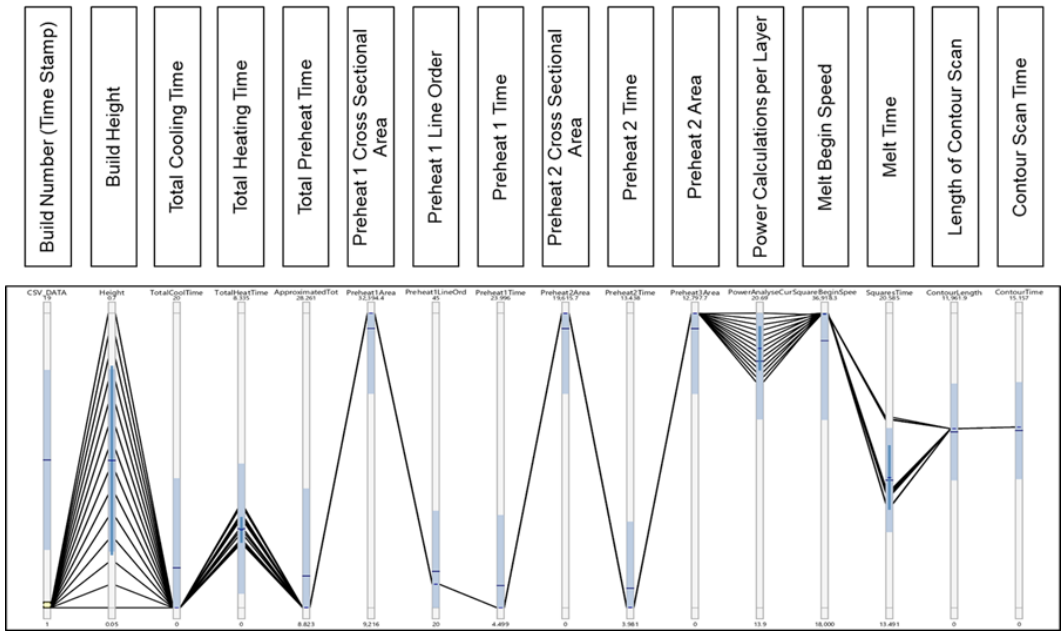

Figure 5: EDEN Interface with Selected Key Variables

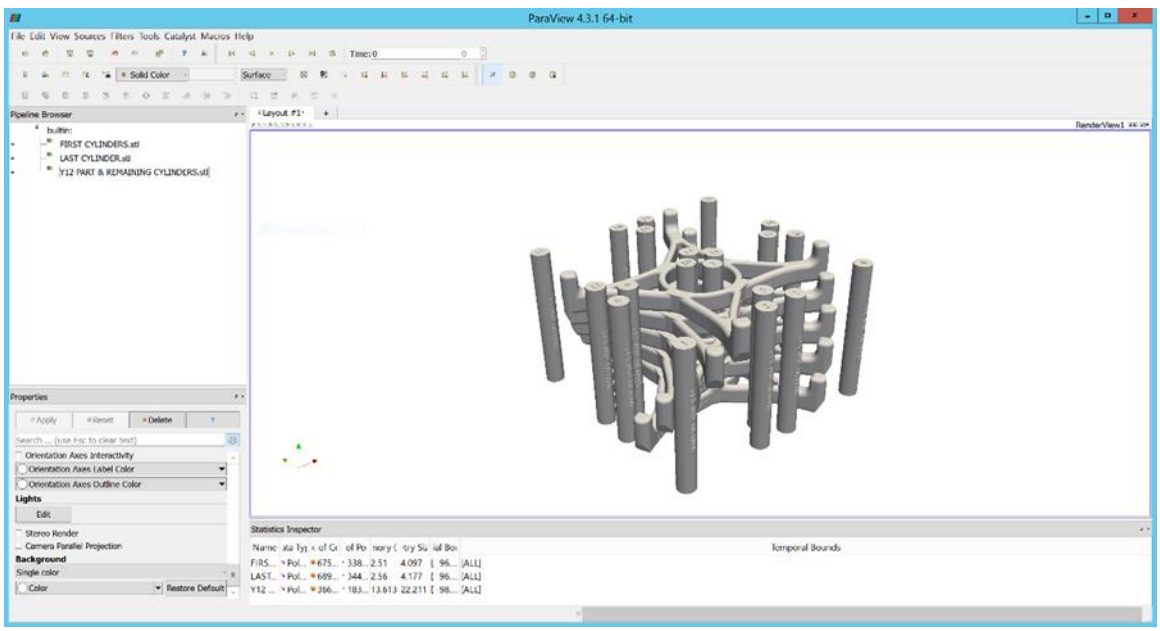

Figure 6: Paraview Interface with Build Layout Setup

Microstructural Characteristics of Ti-6Al-4V

Titanium alloys have desirable characteristics that include high strength, low density, excellent biocompatibility, and corrosion resistance properties. These alloys were well characterized during the mid-1900s such that their applications in the rising aerospace and biomedical industries became standard. This section will provide a brief introduction to the fundamentals of titanium microstructure to understand the scope of the experiments and material characteristics performed in subsequent sections.

Fundamentals of Ti-6Al-4V

As a comparison to other common material systems, Figure 7 shows relevant properties of common material systems for titanium (Ti), iron (Fe), nickel (Ni), and aluminum (Al). These properties include melting temperature, allotropic (phase) transformation, crystal structure, density, mechanical properties, and a comparison of qualitative properties between each system.

In terms of microstructure, the classification of titanium alloys are placed into three categories based on the phases present in the final composition: α phase, dual α+β phase, and β phase [10]. For dual phase α+β, the crystal structure begins with a β phase consisting of a body-centered cubic (BCC) lattice and transforms into the α phase consisting of a hexagonal close-packed (HCP) lattice at temperatures below the allotropic temperature, commonly referred to as the β transus temperature [10]. This process is known as the solid-state phase transformation occuring after the material has solidified from its liquidus state. The unit cells of the α and β lattice are found in Figure 8.

	Ti	Fe	Ni	Al
Melting Temperature (°C)	1670	1538	1455	660
Allotropic Transformation (°C)	$\beta \xrightarrow{882} \alpha$	$\gamma \xrightarrow{912} \alpha$	-	-
Crystal Structure	bcc → hex	fcc → bcc	fcc	fcc
Room Temperature E (GPa)	115	215	200	72
Yield Stress Level (MPa)	1000	1000	1000	500
Density (g/cm^3)	4.5	7.9	8.9	2.7
Comparative Corrosion Resistance	Very High	Low	Medium	High
Comparative Reactivity with Oxygen	Very High	Low	Low	High
Comparative Price of Metal	Very High	Low	High	Medium

Figure 7: Material properties of common materials compared to titanium [10]

The solid-state phase transformation from β to α is highly dependent on chemical composition of the material system. Elements are typically classified as α or β stabilizing elements such that the β transus temperature increases or decreases from 882°C in commercially pure titanium [10].The effect of alloying elements on the β transus temperature is shown in Figure 9 [10]. For the purpose of this study, the chemical composition is fixed for only the well-characterized α+β material system, Ti-6Al-4V. Therefore, the β transus temperature for Ti-6Al-4V is fixed at approximately 920°C.

In titanium alloys, the transformation from β to α can only occur by three specific modes: martensitic, massive, and diffusional transformation [10]. Martensitic (α') formation occurs at cooling rates exceeding 410°C/s such that the α plates nucleate by shear displacive transformation and form long, thin plates grown perpendicular to the prior β grain boundary [11]. This substructure contains a high dislocation density and stacking faults such that mechanical strength rises and ductility suffers [10] [11].

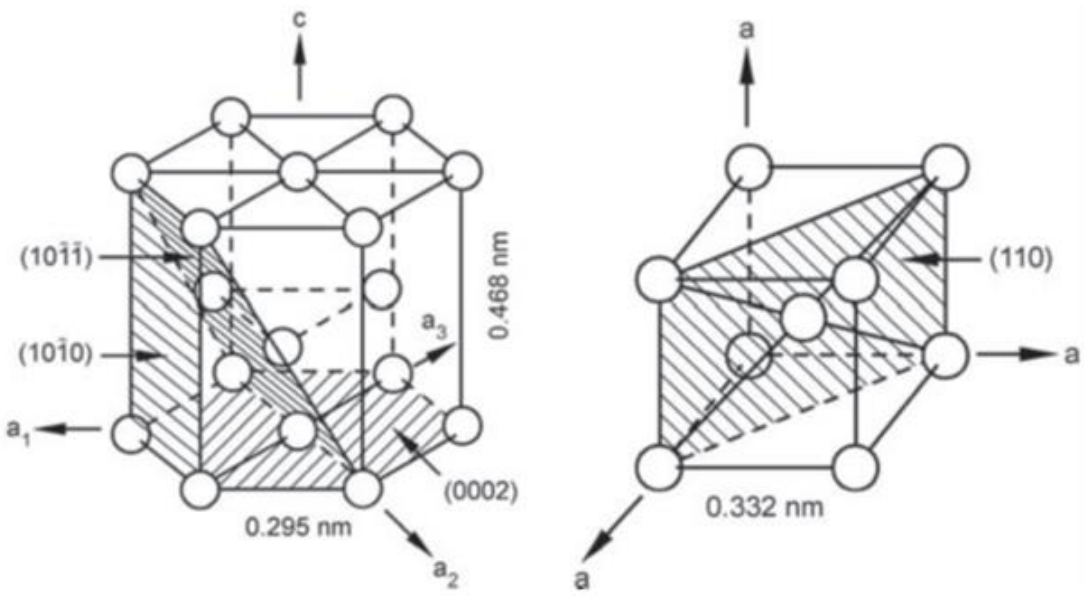

Figure 8: Unit cell of α lattice (left) and β lattice (right) [10]

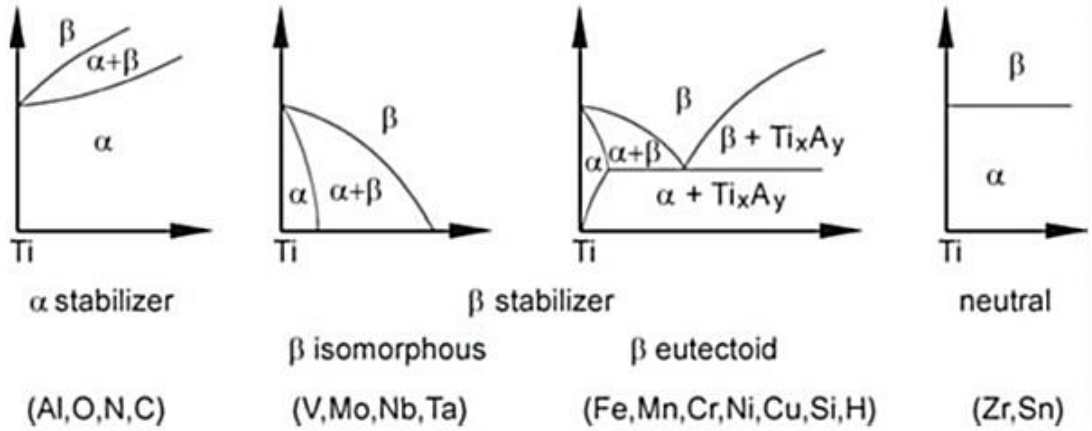

Figure 9: Effect of alloying elements on the β transus temperature [10]

Massive formation (α_m) occurs at cooling rates between 410°C/s and 20°C/s such that regions of parallel α plates form in the same orientation. Figure 10 shows the comparison martensitic and massive α microstructure for continuous cooling at 525°C/s and 20°C/s.

Diffusion occurs at cooling rate slower than 20°C/s from the β phase to the dual phase, α+β, for the traditional microstructure. First, α nucleates along the prior β grain boundary and plates grow orthogonally into the prior β grain. This growth continues until the α plates meet competing α plates from another grain boundary. The resulting microstructure, referred to as Widmanstätten or basket-weave, results in an equilibrium concentration of α and β phases present at room temperature [10]. Figure 11 shows the continuous cooling curves relative to the dominant phases present for the Ti-6Al-4V alloy system.

Widmanstätten microstructure contains a Hall-Petch relationship stating that coarsening of the α plates due to a decrease in cooling rate has a detrimental effect on the strength of the material; as the cooling rate increases, the α plates become thinner in width creating a finer microstructure [12]. This relationship indicates how sensitive phase transformation and resulting microstructure is relative to the cooling curves of the material. Further investigation of Ti-6Al-4V phase transformations and mechanical response follows as it relates to process parameter and build geometry in the E-PBF system.

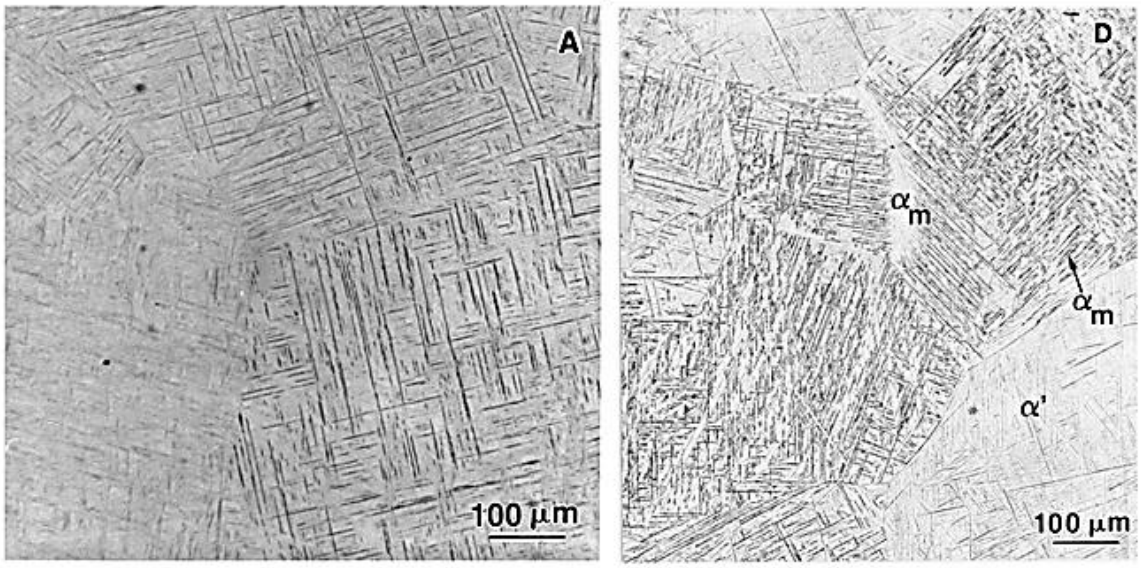

Figure 10: Martensitic (left) and Massive (right) α phases at a cooling rate of 525°C/s and 20°C/s [11]

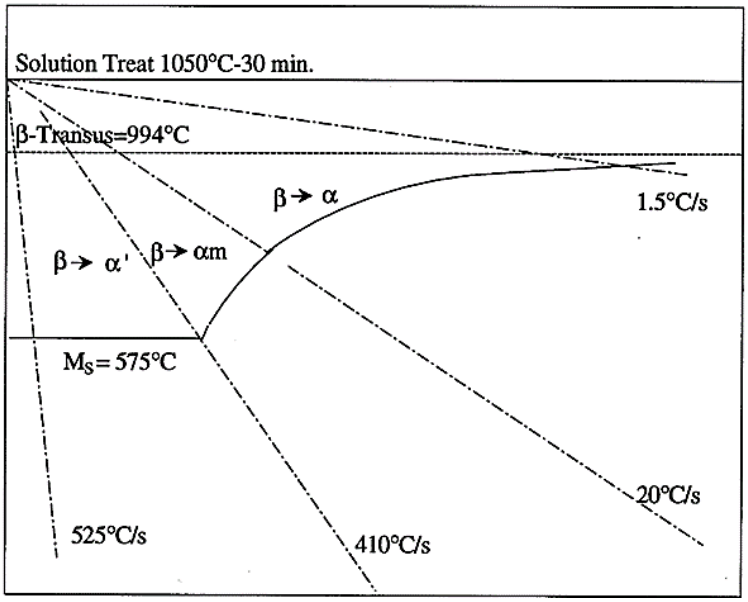

Figure 11: Continuous cooling diagram for Ti-6Al-4V [11]

Phase Transformation of Ti-6Al-4V

Completing a literature review of the commonly observed microstructure present in the E-PBF process, multiple sources have confirmed the absence of α' martensite and the presence of α+β basket-weave in the as-fabricated microstructure l [13][14][15][16][6][17][18][19]. It has been proposed that rapid solidification from the liquidus temperature along with thermal cycling from subsequent layers creates a complex cooling curve as modeled by Tan et al. [13]. Figure 12 shows a schematic phase diagram of Ti-6Al-4V with decreasing temperature compared to the time-temperature plot of the layer being deposited for the nth layer. Stage I of the E-PBF process is the melting event elevating the temperature of the nth layer above the liquidus temperature. Cooling from this stage provides the initial formation of the β grain. Stage II shows rapid solidification for the nth layer to the build temperature and the precipitation of α' martensite from the prior β grain. After powder has been raked over for the $n+1^{th}$ layer, re-heating of the nth layer occurs due to beam penetration for $n+3^{th}$ layers, as seen in Stage III [15]. Subsequent layer depositions thermally cycle the nth layer creating a complex cooling curve for which the final microstructure appears at room temperature [6] [13]. This complex thermal history has been evaluated extensively in the AM community such that links to processing parameters and cooling curves can be found in the following section.

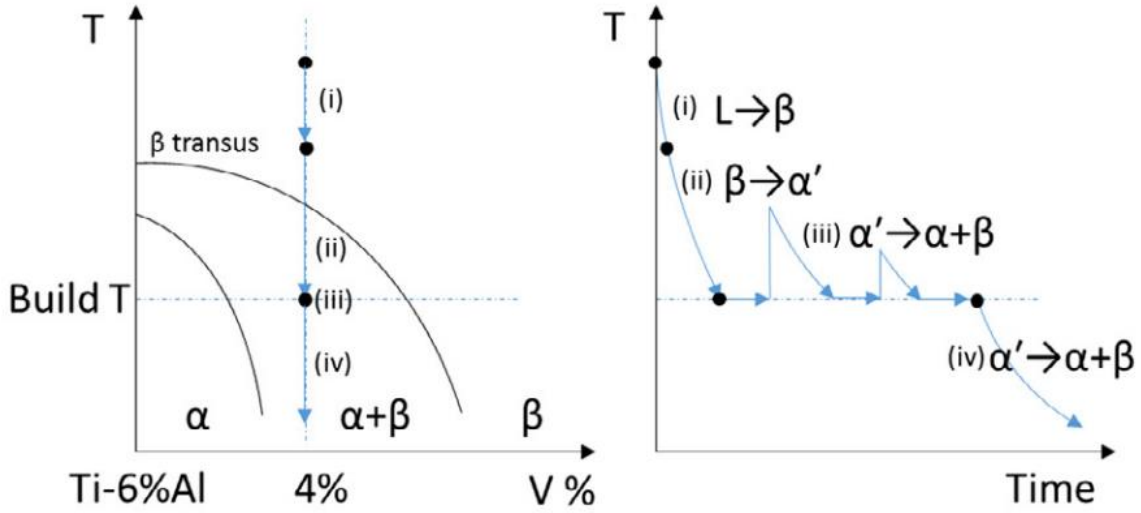

Figure 12: Schematic phase diagram of Ti-6Al-4V (left) and a simplified thermal process showing phase transformation of E-PBF process (right) [13]

Process Parameter Relationships

In terms of microstructural evolutions, two processing conditions, beam power (P) and velocity (V), are required to melt the surface of the material. This is common in welding and AM literature thanks to the Rosenthal equation for temperature profile of a moving heat source based on power, velocity, and material constants [20]. The usefulness of creating a Power-Velocity map can be found in many studies where the microstructure is tailored based on the temperature gradient [15] [21] [22] [23] [24] [25] [26] [18] [7] [27] [28]. In the E-PBF process, changing the energy applied can be achieved by countless variables such as preheat current, beam current, focus offset, speed function, and line offset. Many authors have used this approach to modify microstructure and optimize for density.

Gong et al. looked to generate an optimum processing window by manipulating line offset and focus offset in order to create fully dense, non-porous cubes [24]. Narra et al. used the manipulation of beam current, speed function, and focus offset to control the melt pool and beta grain size in the as-fabricated material [29]. Seifi et al. shows the deviations for the optimum condition in the P-V space can results in under melting (lack-of-fusion, LOF) and over melting (swelling, beading) occurring [30]. Al-Bermani et al. changed the preheat current to vary the build temperature for a constant cross section geometry [15]. Each of these studies use a different method of energy manipulation to achieve a change in microstructure. This leads to the question are any process parameters linked together and how confident are researchers in their results.

Mechanical Behavior of Ti-6Al-4V

The most influential microstructural parameter on the mechanical properties of the α+β microstructure is the α colony size, which is controlled by the cooling curve from the β phase [10]. The α colony size is measured as the width of the individual α plates taken from SEM images [10]. Restated, this means that for a finer α+β microstructure, the yield strength of the material increases while coarser microstructure causes yield strength decreases. Figure 13 shows this relationship graphically for common α+β alloys.

This relationship occurs consistently when loading in tension such that correlations to microstructure from bulk mechanical testing is possible. However, the introduction of defects provides additional challenges related to stress concentration. Due to the irregular shape, stress concentrates at the corners of defects when loading the material. Defects serve as likely failure initiation locations for tensile testing and crack

initiation sites in fatigue testing. These sites initiate only when there is a consistent surface finish as conducted through ASTM E8 standard. Three separate studies show the failure characteristics of lack-of-fusion defects related to fatigue life in E-PBF of Ti-6Al-4V [31] [14] [24]. Countless other studies have been performed across other materials and powder bed fusion processes.

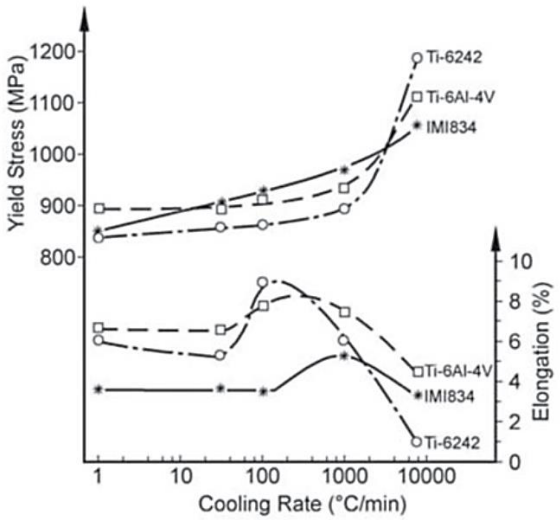

Figure 13: Effect of cooling rate from the β phase on yield strength and elongation [10]

Relevance to Current Work

As a result of an extensive literature review, this study will focus predominately on the α+β basket-weave microstructure of Ti-6Al-4V for the E-PBF process. In this process, changing the applied energy can be achieved by modifications to many process parameters, as seen previously. However, the range of parameters that influence energy input is not fully characterized. Determination of key process variables is almost as important as the processing steps itself [32]. Therefore, it is vital to provide a map for processing parameters such that researchers have more confidence in the conclusions provided by their experiments. Based on the results of mapping process parameters, a reliable mechanism for modifying the build temperature and subsequent energy input is by varying the surface temperature. This work explores the possibility to modify the cooling curve and microstructure of the material without imparting changes on the build setup or other process parameters. Since the cooling curve is very complex, the ranges of heating and cooling applied to the end of each layer along with estimates of the cooling curve for each sample provide the necessary background for process controlled microstructure.

It was previously proposed that these complex thermal cycles can create differences in microstructure such that banding may be present [6]. Graded microstructure appears in studies by Tan et al. in the E-PBF process and by Kelly and Kampe in the directed energy deposition process due to variation in cooling curves in Ti-6Al-4V [13] [33]. Two methods to vary cooling curves in the E-PBF process are changing build setup and changing processing conditions. Part 2 investigates the effects

that melt order, part proximity, and build volume has on the cooling curves of as-fabricated tensile bars. In this experiment, the samples tested in tension were created in the as-fabricated condition under the assumptions that finer microstructure will generate high yield strength and defects will indicate likely locations for failure to occur.

CHAPTER THREE

EXPERIMENTAL PROCEDURE

Each of the following subsections breaks down the experimental setup, sample preparation, and data collection. First, the experimental setup is explained in detail. Next, the procedure for bulk material characterization is detailed for polishing, etching, imaging, measuring hardness, and mechanically testing samples. Finally, the procedure for collecting and analyzing in-situ data such as near infrared (NIR) images and log file data is explained.

Experimental Setup

All components for this study were fabricated using the Arcam Q Plus Series E-PBF machine (R1119) at the Oak Ridge National Laboratory Manufacturing Demonstration Facility (ORNL MDF). Each build was completed on a 210 by 210 mm start plate using plasma atomized powder provided by Tekna. The Q-series machine utilizes the latest technology from Arcam AB with upgraded hardware and software, build simulations, LayerQam near infrared (NIR) images, and log file data. These tools are useful in characterizing the as-fabricated state and rationalizing results from bulk material characterization. Machine certification and build setup was completed per Arcam specifications to ensure build quality and consistency over the course of these experiments.

In the first part of this study, the simulation feature of the Q-series system was used by inputting a build layout with selected process parameters and outputting log file

variables. This feature allows the machine to create the scan strategy and build the heat model associated with the input process parameters. This simulation ensures the machine can successfully analyze the layout before starting the build. Eighteen process parameter inputs were modified and the simulation feature was used to generate log files for analysis. These changes in process parameters are referred to as sets where Set 1 contains the standard process parameters given by Arcam AB and Sets 2 through 19 contain changes to the selected variables. A standard Arcam layout was used for processing such that the cross section of each layer is identical over the 15 collected layers, as seen in Figure 14A/B. The resulting log files were visualized and analyzed to determine which of the process parameters are connected to each other. Each of the changes made to process parameters are presented in Table 1 while the software and melt themes used in mapping the process parameters are presented in Table 2 below.

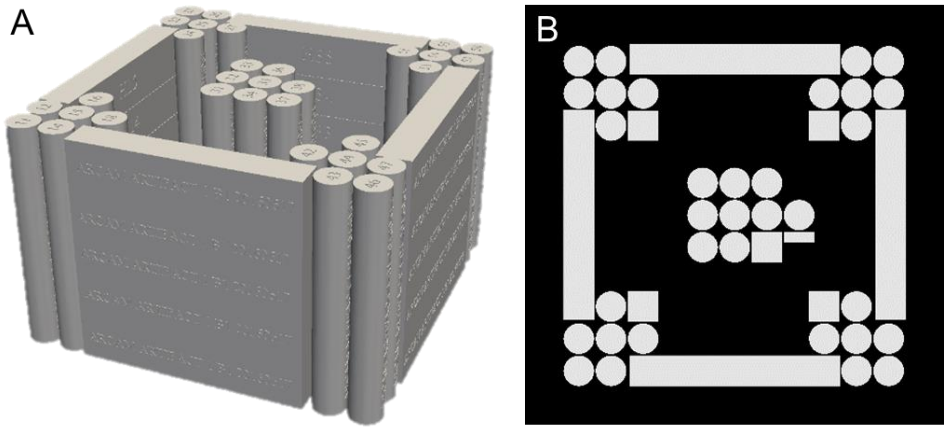

Figure 14: Arcam Test Artifact Layout (A) with one image of the total build cross section (B)

Table 1: Software version, processing themes, and powder used for Process Parameter Mapping

Process Parameter Interconnectivity Setup	
Software Version	EBM Control 5.2.23
Themes – Preheat, Melt	5.2.23, 5.2.23
Powder (Lot Number)	--

Table 2: Set list of process parameter changes

Process Parameter	**Standard Value**	**Changed Value**
Post Heat Max Time	20	10
Preheat Square Auto Box Calc	True	False
Preheat I Max Beam Current (mA)	16	32
Preheat I Max # of Reps	20	40
Preheat II Max Beam Current (mA)	19	38
Preheat II Average Current (mA)	5.4	8.0
Preheat II Heater Current (mA)	48	30
Melt Power Temperature	940	840
Melt Power Min Current (mA)	3	10
Melt # of Contours	3	5
Melt # of Contours	3	0
Melt Hatch Offset to Contour	0	-1
Melt Hatch Use Rotating Hatch	True	False
Melt Square Rotating Angle per mm	1350	750
Melt Beam Speed Function	60	72
Melt Beam Focus Offset (mA)	36	24
Melt Hatch Square Thickness	True	False
Melt Optimize Optimal Hatch Length	62	75

Based on the results of modifying process parameters, a preliminary exploration of the surface temperature variable was conducted to determine if could be used to control microstructural evolution in Ti-6Al-4V. In the previous build, samples were arranged randomly in the build chamber and supported accordingly to ensure build success, known as ORNL TA2. However, samples fabricated at the top and bottom of the build chamber contained different microstructure. Therefore, by altering the surface temperature values, this study looked to alter the heating and cooling stages of the melt and possibly the cooling curves for each sample. An isometric view of ORNL TA2 is shown, Figure 15, for both the control build and the variable surface temperature build. This geometry contains varying cross-sectional melt area from high to low in colors red, green, yellow, blue, respectively. The microstructure of two characterized bars, Sample 11 in red and 18 in yellow, varies for each region. In this experiment, the build was broken into four separate STL files for the corresponding color regions as shown in Table 3, below. Samples 11 and 18 were cut, mounted, polished, and imaged according to the microstructural characterization process to determine if the changes in surface temperature altered the microstructure. The software version, processing themes, and powder used in modifying the surface temperature are presented in Table 3 below.

The second task in the study is to determine the effectiveness of current qualification techniques related to build setup. The changes in build setup vary part melt order, build volume, and total cross-sectional area. This experiment validates traditional qualification methods by varying build setup and showing the results of data analytic

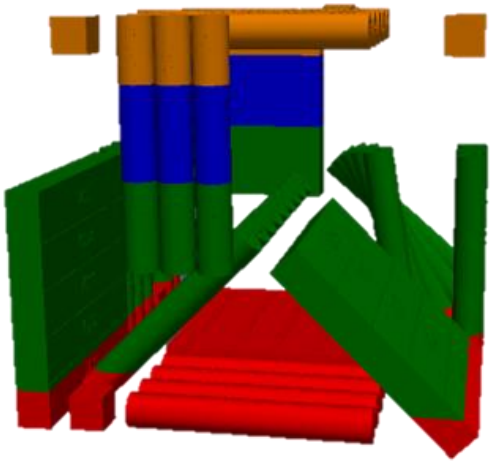

Figure 15: ORNL Test Artifact 2 Layout with Varying Cross-Sectional Melt Area from High (Red) to Low (Blue)

Table 3: Software version, processing themes, and powder used for Process Controlled Microstructure

Process Controlled Microstructure Setup	
Software Version	EBM Control 5.2.23
Themes – Preheat, Melt, & Wafer	5.2.23, 5.2.23, 5.2.23
Melt Section 1	Surface Temp – 820 (11, 12, 14, 15, H11-15, H31, H21)
Melt Section 2	Surface Temp – 800 (31-38, 45, 51-57, H22-25, H32-35, H41-42)
Melt Section 3	Surface Temp – 800 (44, 46, 47, H43-44)
Melt Section 4	Surface Temp – 780 (16, 18, 24, 42, 43, H45)
Powder (Lot Number)	Tekna Ti-6Al-4V (33306-16-004)

tools. The isometric and top view of the build layout along with changes to the support spacing between Build 1 and 2 are presented in Figure 16. Only the effects of build setup were evaluated on the twenty fabricated bars and not the central parts. This isolates the consistent part geometry and exaggerate the effects caused by the central parts on the fabricated bars. The software, melt themes, and powder used in part 2 are presented in Table 4 below. To for melt order, each fabricated part was separated into three melt orders as seen in Table 4 and visually in Figure 16A, where yellow, green, and blue indicates melt order 1, 2, and 3, respectively. Each part in a melt order was then loaded as a single melt theme on the machine to confirm that all parts in that melt order were printed before moving to the next order. For example, tensile bars five, six, fifteen, and sixteen were loaded together with the five fixtures such that they would be melted second in order. This layout was repeated for both builds keeping the order of the parts the same. The sole difference between Build 1 and 2 is the change in support structure height between the central fixtures from 1.6 to 4.1 mm, as seen in Figure 16B. Due to the change in total build height, the height of the fabricated bars increased from 102 to 114 mm. It is important to note that even though the bars increased in height, all the tested tensile bars for both builds came from the bottom 76 mm of the fabricated bars, as mentioned in the materials characterization section below.

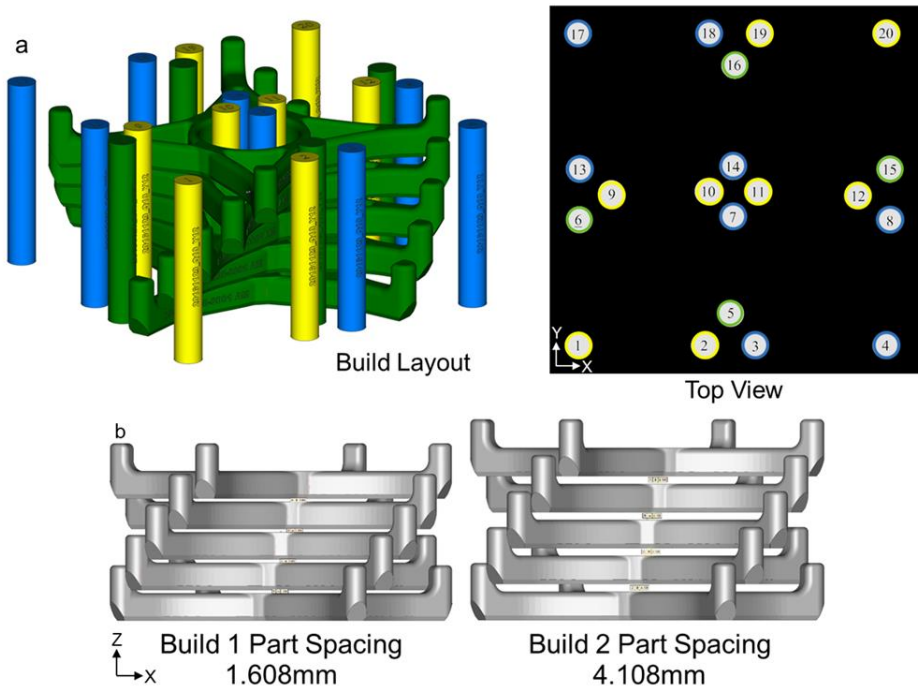

Figure 16: Build Layout isometric and top view (A) where yellow, green, and blue signify melt order 1, 2, & 3, respectively. (B) Side view of fixture spacing to show changes in part spacing between Build 1 and 2

Table 4: Software version, processing themes, and powder used for Build Layout Variation

Build Layout Variation Setup	
Software Version	EBM Control 5.0.57
Themes – Preheat, Melt, & Wafer	5.0.57, 5.0.57, 5.0.57
Melt Order 1 Samples	Bar # 1, 2, 9, 10, 11, 12, 19, 20
Melt Order 2 Samples	5 Fixtures & Bar # 5, 6, 15, 16
Melt Order 3 Samples	Bar # 3, 4, 7, 8, 13, 14, 17, 18
Powder (Lot Number)	Tekna Ti-6Al-4V (33306-16-004)

Materials Characterization

Polishing & Etching Techniques

All samples used for microstructural characterization were polished to a mirror finish according to the Kroll's procedure with etching of reagents to exaggerate the grain structure for microscopy. These polished and etched samples were necessary to characterize the microstructure of the materials in the as-fabricated condition to rationalize results of each sections experiments. This polishing procedure was used for all shown images of microstructure and hardness throughout this thesis.

Microstructural Imaging & Measurements

In order to characterize the microstructure of the materials, a Hitachi TM 3030 Plus Scanning Electron Microscope (SEM) was used to image the surfaces of the polished samples. Measurements of the α plates were completed using the SEM images taken at a magnification of 5000x and ImageJ to match the scale of the image with the perpendicular line measuring the width of the α plates. This imaging and measurement procedure was used for all shown images of microstructure throughout this thesis. The microstructural characterization was completed using a Leica DM400 M LED optical microscope while the hardness measurements used a Leco LM110AT tester with 300 grams of force to generate a map of hardness values. Hardness measurement tests were completed to the ASTM 384-16 standard to ensure consistency [34].

Tensile Testing

For all uniaxial tensile testing results shown, the conditions of the test were completed in accordance with ASTM E8/E8M-16a under strain-controlled loading of 0.005mm/mm/min at ambient temperature [35]. Each tensile bar was machined from the bottom 76 mm of the as-fabricated bars for consistent gage locations. Each gage section contained two regions where minimal melting of the central parts occurs. All testing was completed at Sintavia (ISO 17025 Certified) on an Instron 300kN load frame.

CHAPTER FOUR

RESULTS AND DISCUSSION

This section highlights the results of interest for each of the experiments performed in this study. As mentioned previously, Part 1 looks at the interconnectivity of the log file parameters by varying a key process parameter and measuring the response. This experiment focuses on the data tool, EDEN, for analysis and comparison. A preliminary investigation of the surface temperature variable is completed to determine the usefulness in modifying microstructure. Part 2 evaluates build setup variables such as melt order, part proximity, and build volume on the cooling curves of tensile bars. These bars are tested in uniaxial tension and data tools are used to rationalize the results.

Process Parameter Mapping for Process Controlled Microstructure

Due to the extensive nature of the search, all sets named in Table 2 are not evaluated either redundancy of the results between sets. However, four of the most impactful results are analyzed in depth. The first set comparison is between Set 1 and Set 2 where the post heat time is reduced from 20 seconds to 10 seconds, as seen in Figure 17. This comparison reveals that there are no changes in the visualized variables such that the trend in the two data sets are identical. This occurs due to the geometry and the heat model of the selected layers being analyzed. By looking at column 4 in Figure 17, the maximum heating time reached for the standard melt themes, Set 1, is only 3 seconds. This indicates the maximum post heat time never reaches the threshold of 10 seconds as required by Set 2. However, if this threshold was required to be less than 3 seconds, the

build would be limited to the new threshold. Setting this threshold lower than required can be useful in reducing over heating of the part surface that may lead to swelling. Care should be made when setting this value as the cooling curve of the material can be affected due to decreased energy input at the end of the layer, which may alter the microstructure.

The second set comparison, Figure 18, is between Set 1 and 16 where speed function is reduced from 60 to 72. As shown in Chapter 2 Background and Literature Review, this is a common practice in the E-PBF community to tailor the microstructure based on the shape and depth of the melt pool. Therefore, it bodes well that the only changes made in the analyze calculations are in column 14 melt time. As the speed function increases, the melt time decreases since the melt is occurring faster over a constant cross-sectional area. This is most impactful when comparing literature values for changing speed function such that the speed function is only proportional to the changes in melt pool shape and depth.

The third comparison set, Figure 19, is between Set 1 and 12, where the contour step is effectively removed by changing the number of contours from 3 to 0. As seen in a study from Cordero et al. presented in Chapter 2, increasing the number of contour passes can smooth the surface of the as-fabricated material while reducing the possibility of forming chimney porosity [22]. However, those looking to optimize build times may elect to reduce the number of contours or eliminate them altogether. Figure 19 shows the resulting calculation made by removing the contour stage. In columns 15 and 16 on the right of the figure, you can see an indicated drop in contour time and length from a

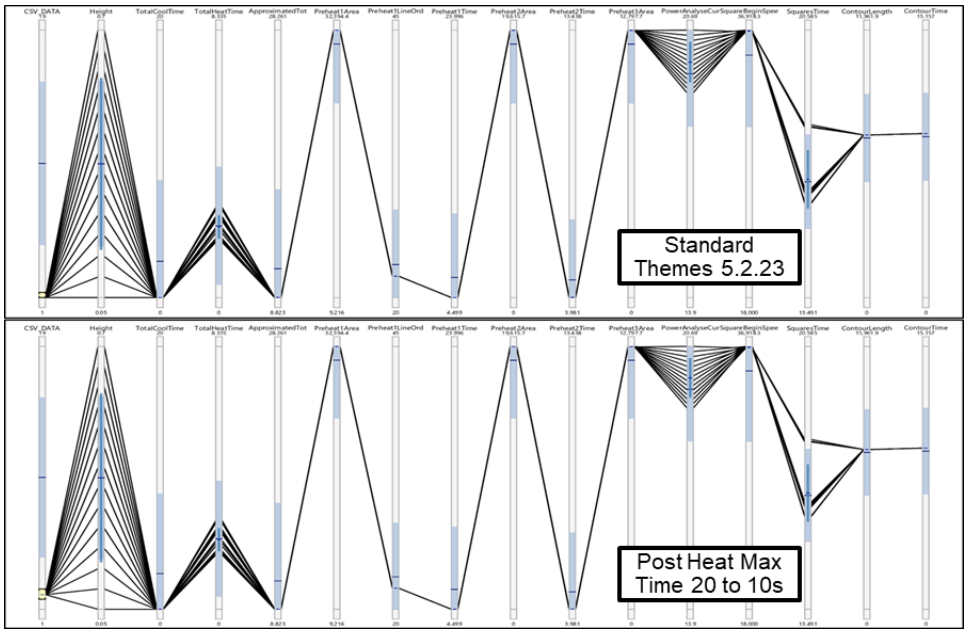

Figure 17: Comparison of Set 1: Standard Melt Theme (Top) and Set 2: Reducing the Post Heat Time (Bottom)

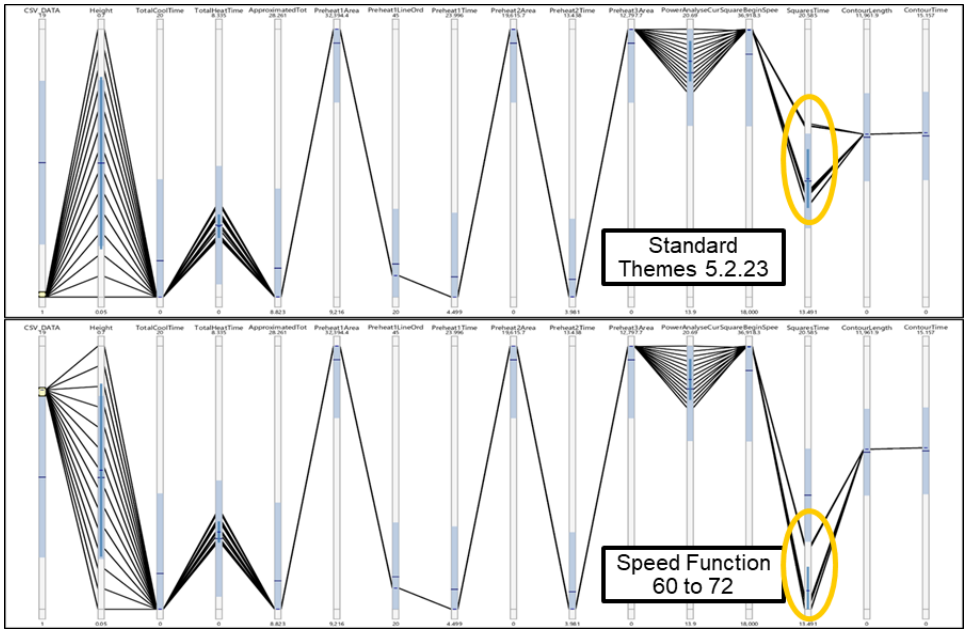

Figure 18: Comparison of Set 1: Standard Melt Theme (Top) and Set 16: Increasing Speed Function (Bottom)

constant value to zero. This confirms the software is removing the contour step from its calculations. By looking just to the left in column 14, Figure 19 shows an increase in the melting time such that the area lost by the contour stage is now gained by the melting stage to reach the dimensional accuracy. This is confirmed from the preheat area calculations, columns 6 and 9, remaining constant over the changes in the melting stage. The final indication in this figure shows a change from post heating to post cooling in columns 4 and 3, respectively. This change is related to the heat model calculations where the time required to print the contours requires additional heat. Therefore, if the manufacturing goes from adding heat at the end of the layer to passively waiting, the cooling curve for each part has now changed which can influence the evolution of the microstructure over the course of a build.

The fourth comparison set, Figure 20, is between Set 1 and 9, where the analyze power calculation temperature is reduced from 940 to 840 effectively modifying the equilibrium temperature that the heat model requires. It is important to see which variables are affected by the changes in temperature value and if this can be useful in altering the microstructure. Here, we can see that the only changes in the analyze calculations come from columns 3/4 and 12 for post heating/cooling and the analyze power energy. The power energy variable reduces by 25% for a 100-degree change in surface temperature while the post heating changes to a post cooling stage. Since this change only affects the internal heat model and no other present variables, it has potential to change the cooling curve of the material without influencing the rest of the process parameters. The results of the other sets can be found in Appendix A.

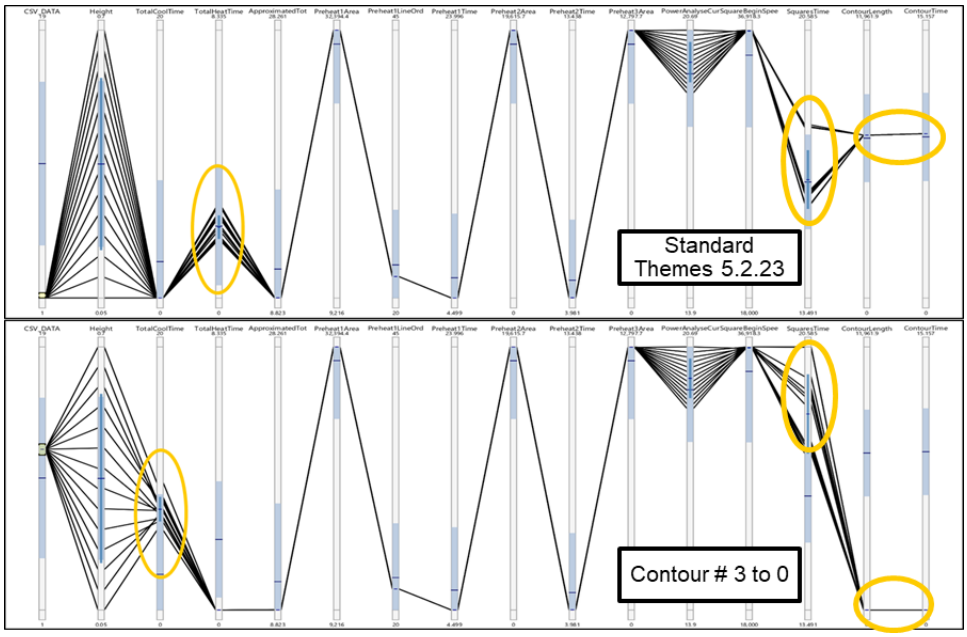

Figure 19: Comparison of Set 1: Standard Melt Theme (Top) and Set 12: Removing Contours (Bottom)

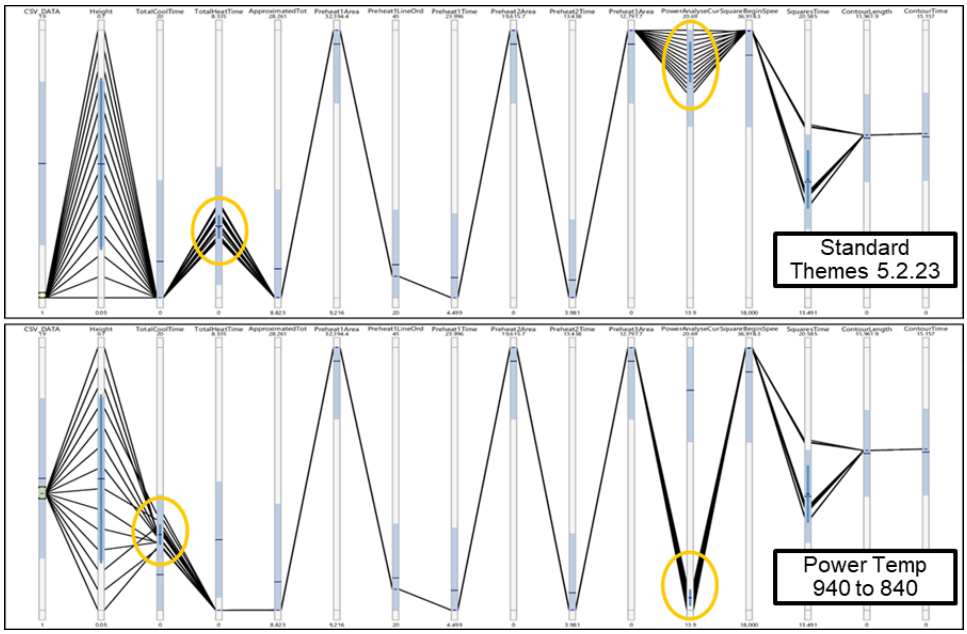

Figure 20: Comparison of Set 1: Standard Melt Theme (Top) and Set 9: Reducing Power Temperature (Bottom)

It was previously determined that by modifying the surface temperature variable, no other variables were influenced and the heating and cooling values correlated with changes in the surface temperature. This work provides a preliminary investigation into controlling the microstructure in the as-fabricated condition such that the surface temperature can be related to cooling curves.

First, it is necessary to understand the bounds of the surface temperature variable and determine how changes will affect the heating and cooling calculations. Using the same technique discussed previously, log files with surface temperatures ranging from 740 to 1000° C were simulated for a single layer. The associated heating and cooling values are plotted in Figure 21. This plot is useful in determining how much energy is applied at the end of the layer such that a prediction about the cooling rate can be made.

In order to determine the effectiveness of this parameter, two builds were completed to compare the microstructure of the samples 11 (bottom, red) and 18 (top, yellow). For comparison, Sample 11 was attached to the build plate on minimal support structure such that the cooling rate is expected to be very fast. Sample 18 was floating in the powder bed with 30 mm of support structure attached that did not allow for heat to flow to the start plate. This would expect the cooling rate of Sample 18 to be much slower than that of

Sample 11. In Build 1, the geometry was unable to completed by standard processing themes due to swelling of the parts surface; therefore, the heating and cooling functions were turned off and the build was successfully completed with no heating or cooling applied at the end of each layer. In Build 2, the surface temperature was lowered

according to each melt theme section shown in Table 3, above. For the samples of interest, Sample 11 (bottom, red) was fabricated in melt theme one with a surface temperature of 820 while Sample 18 (top, yellow) was fabricated in melt theme four with a surface temperature of 720. Figure 22 compares the base microstructure with no heating and cooling to the modified melt theme for Samples 11 and 18. It is apparent that the microstructure and cooling curve for the base microstructure is vastly different. Sample 18 mimics a slow cooling, coarse microstructure. In contrast, Sample 11 from the base themes has a much faster cooling rate producing a fine microstructure. However, in an attempt to make them uniform, the modifications to the surface temperature variable for B2 creates a microstructure similar to that of a fast cooling curve. Based on these images, it is possible to conclude that modifications to the surface temperature can have dramatic effects of the microstructure of the samples; however, this is only preliminary work such that controlled characterization must be done to further understand this phenomenon.

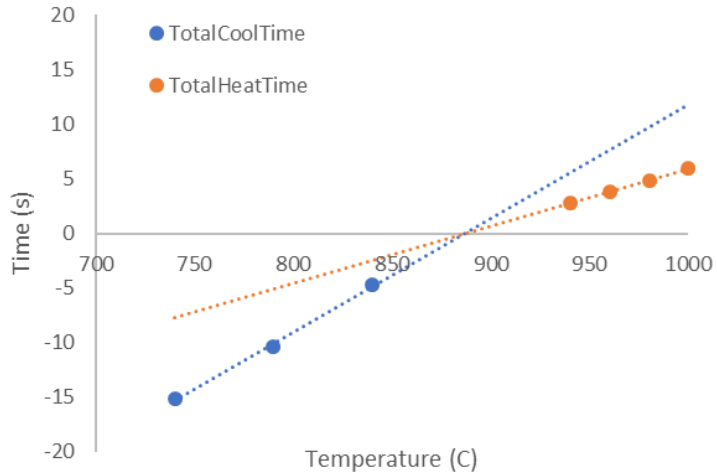

Figure 21: Post Heat/Cool Time versus Temperature plot for varying surface temperature values

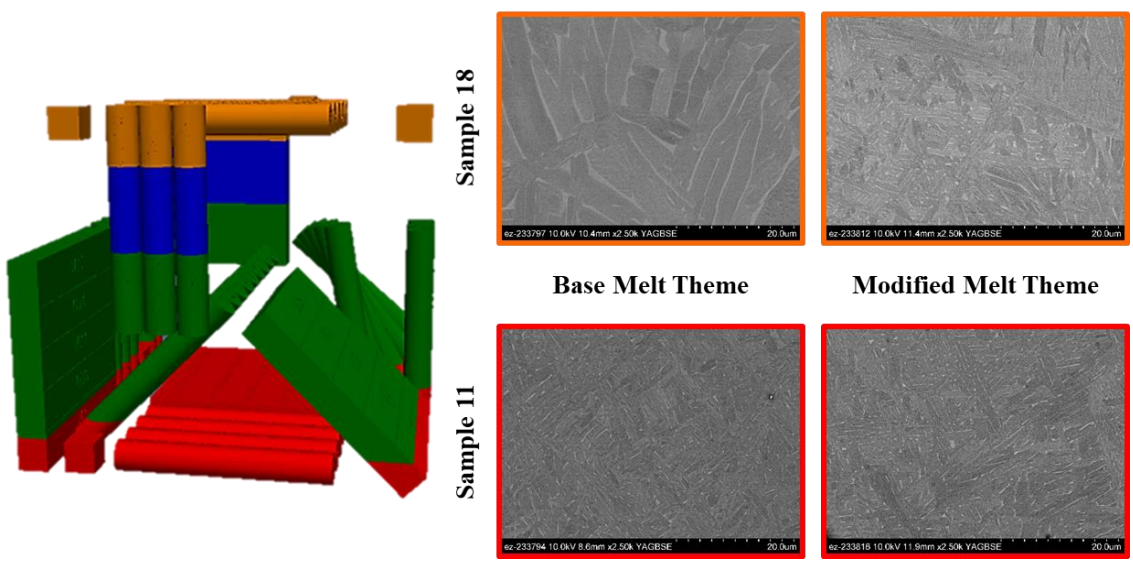

Figure 22: Comparing Samples 18 (Top) and 11 (Bottom) between the standard and modified melt themes

Build Setup Variable Evaluation

In Part 2, this study looked to test the effects of build setup variables on the mechanical performance of as-fabricated tensile bars in two representative builds. These build setup variables include changes to setup such as melt order, build volume, and total cross-sectional area. The first part of the experiment is to evaluate the mechanical response of the melt order variation. For both builds, eleven of the twenty printed bars in the build chamber were tested in uniaxial tension such that all melt orders were evaluated. Figure 23 shows the yield strength versus the sample number with a tested sample labeling scheme of Build Number – Melt Order-Sample Number. Melt order is separated for ease of visualization where first, middle, and last melt order is colored in yellow, green, and blue, respectively. By comparing samples printed between melt orders, the data shows that the melt order has no dependence on the yield strength. Samples 2L-18 (Melt Order 3) & 2F-19 (Melt Order 1) were observed under a SEM, as seen in Figure 24. Measurement were taken of the α-laths, see Table 5, to confirm that the underlying microstructure between each sample is similar. These measurements and yield strength values confirm that the melt order plays no role in the evolution of microstructure. To rationalize these results, it is worth understanding the nuances of the proprietary heat model and how it is able to recognize each melt order as an independent group. For example, Arcam explains when melt order one finishes, the model requires a post heat to be applied to the entire surface before the next melt order begins [5]. The surface temperature of all printed parts is brought back to the desired surface temperature indicated in the melt theme (920°C for all). Once the surface of all melted regions

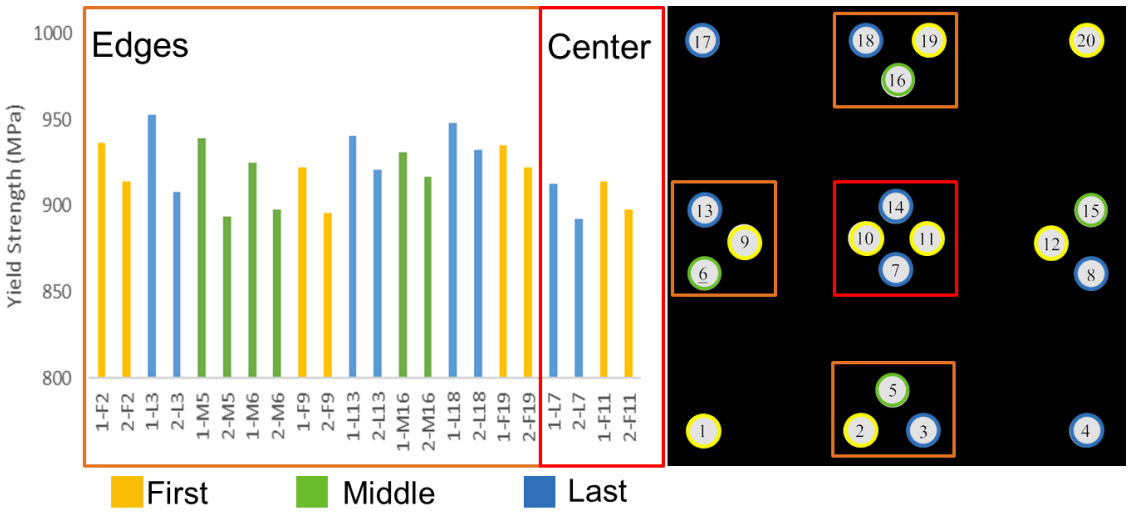

Figure 23: Uniaxial yield strength (MPa) results broken down by sample and x-y location on the start plate. Colors indicate melt order where yellow, green, and blue are order 1, 2, & 3, respectively. Sample labeling as follows: Build Number – Melt Order-Sample Number

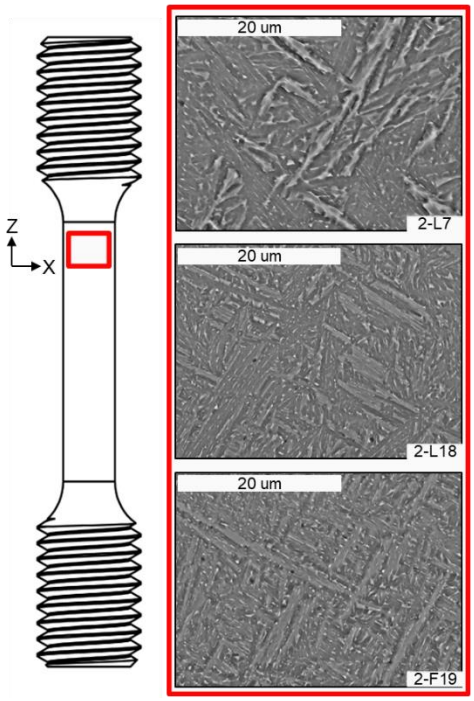

Figure 24: X-Z micrographs of tested samples showing change in microstructure from top to middle (2-L7 & 2-L18) and similarity from middle to bottom (2-L18 & 2-F19)

Table 5: α – Lath measurements of samples shown in Figure 3 & Figure 6 comparing Melt Order, Sample Location, and Build Number

Sample	Average Lath Measurements
2-L7 Top Thread	0.81 ± 0.121
2-L18 Top Thread	0.56 ± 0.093
2-F19 Top Thread	0.60 ± 0.111
1-L18 Top Stock	0.54 ± 0.102
2-L18 Top Stock	0.68 ± 0.129

achieves the desired 920°C, powder for the next layer is raked over and the uniform cooling curve dictates the evolution of $\alpha + \beta$ microstructure and the coarsening of the α laths. Therefore, small changes in the cooling conditions are not observed in either the yield strength or microstructure when comparing the order in which parts are melted.

Further investigating Figure 23 shows that the mechanical properties vary relative to their location on the start plate. The highest, 932 MPa, and lowest, 892 MPa, yield strength values are come from samples 2L-18 at the edge and 2L-7 at the center. The variation in microstructure appears in Figure 24 with measurements found in Table 5. By looking back at Figure 23, Samples 7, 10, 11, and 14 were all printed inside the central holes of the fixtures where other samples have more room between samples. It is hypothesized that the heat of the powder bed is retained in the central samples as compared to those on the edges due to the proximity of the parts printed near it. This hypothesis is confirmed by the study from Hrabe et al. where proximity of printed parts influenced their mechanical performance as well [7].

Another trend observed in Figure 23 shows that samples tested in Build 1 failed at a higher yield strength than those the same samples tested in Build 2. Figure 25 plots the yield strength versus elongation of all tested samples while Table 6 shows the t-test statistical results of tensile, yield strength, and elongation. The statistical tests confirm that the yield strength and elongation between builds are statistically different (less than 0.05 unpaired T-test). However, the role of elongation in the as-fabricated samples will be discussed in later sections with NIR image analysis. The statistical difference in yield strength as a function of build can be rationalized by looking at the Figure 26 plots the bottom temperature profiles. Build 2 was under processing for almost 6 hours longer for an increase in only 10 mm. It is hypothesized that a hold at low temperature due to thermal cycling is reflected at the end of the temperature plot. Here the bottom temperature readings from Build 1 and 2 cross and Build 2 holds at temperature for longer time. This temperature hold produces a coarser microstructure in Build 2, which can be attributed to lower yield strength. To confirm the coarsening of microstructure between Build 1 and 2, Figure 27 and Table 5 shows a comparison of the microstructure from tested Sample 1-L18 and 2-L18. This indicates that increased build height due to changes in support length between fixtures has a statistically significant impact on yield strength all samples.

Now that we have concluded our analysis of the mechanical properties, this study shifts focus to the value of collecting in-situ layer images for correlation to mechanical results and porosity distributions. Since both builds show identical trends in NIR image analysis, the following discussion focuses on the observations solely from Build 2. NIR

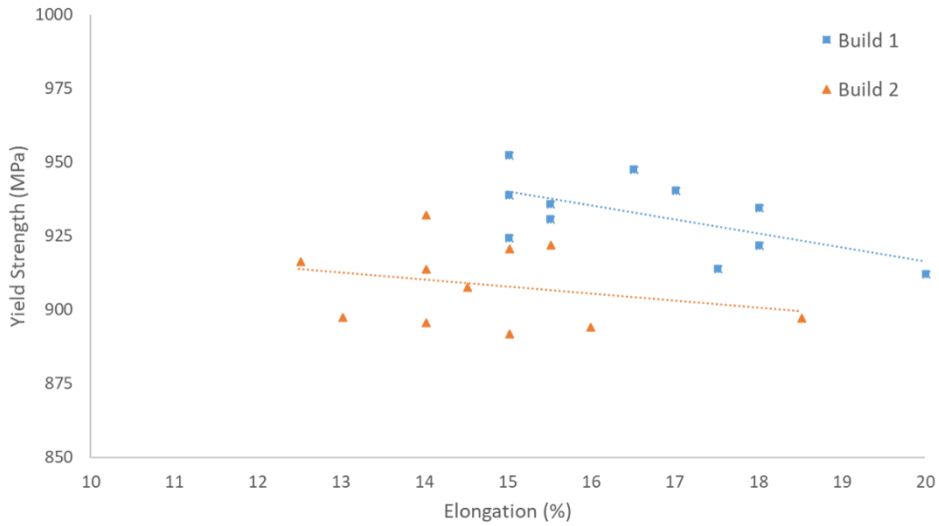

Figure 25: Yield Strength (MPa) versus Elongation (%) of Samples Tested in Build 1 (Blue Squares) & Build 2 (Orange Triangles)

Table 6: Mean, Standard Deviation, and Unpaired T-Test of tensile testing results comparing Ultimate Tensile Strength, Yield Strength, and Elongation between Build 1 & 2.

	Ultimate Tensile Strength (MPa)		**Yield Strength (MPa)**		**Elongation (%)**	
	Average	**Std**	**Average**	**Std**	**Average**	**Std**
Build 1	1027.7	12.76	932.6	12.96	16.6	1.63
Build 1	1019.9	14.17	910.5	13.79	14.7	1.62
Unpaired T-test	0.1931		0.00045		0.0121	

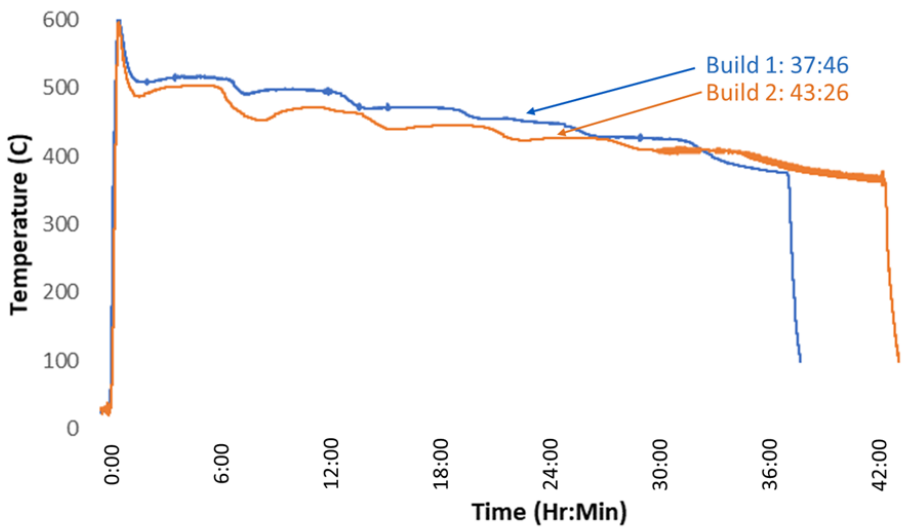

Figure 26: In-situ collected bottom temperature (C) for Builds 1 & 2 with total printing time in hh:mm

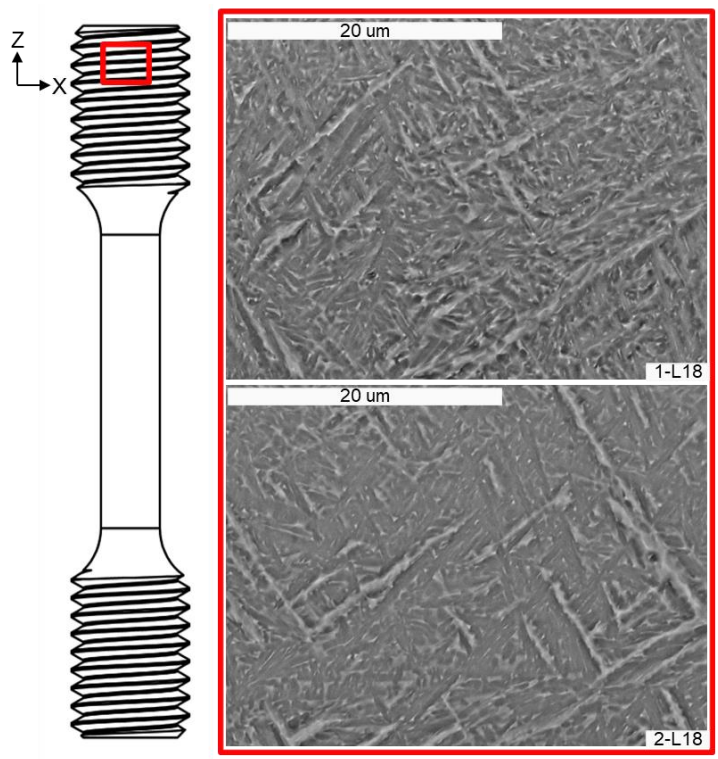

Figure 27: X-Z micrographs of tested samples from Build 1 (1-L18) to Build 2 (2-L18)

images were collected for each layer in two modes: constant exposure and automatic exposure. Constant exposure allows no skewing of the pixel intensity between layers such that the intensity may be related to the surface temperature of the part before raking occurs. This image collection method is be useful in determining the correlation of mechanical properties to pixel intensity. The second captured image is automatic exposure where the machine software obtains multiple exposure images and selects the optimal image for feature recognition analysis. This image set is used to resolve internal features and correlated to part failure.

Figure 28a shows a visual reconstruction of the constant exposure NIR images for each tensile bar and plots the pixel intensity versus layer height. Each sample labeled and plotted in green corresponds to the higher pixel intensity. In contrast, those labeled and plotted in orange corresponds to lower pixel intensity parts. It is easy to see that the parts located in the center of the plate correspond to a higher pixel intensity while the parts on the edges correspond to a lower pixel intensity. In Figure 28b, the mechanical properties of the central parts in green circles and the edge parts in orange triangles are color coded to match the pixel intensity plot.

Figure 28 suggests that the samples containing the highest pixel intensity are related to higher surface temperatures, coarser microstructure, and lower yield strength. If true, the use of NIR pixel intensity may determine mechanical properties relative to parts inside of the build chamber. However, several lower pixel intensity samples (5, 6, 9) contain lower yield strength similar to higher intensity samples (7, 11) contradicting this conclusion. One source of error in evaluating the constant exposure NIR images comes

by remembering the melt order role in this study. The parts melted in the first melt order contain a lower pixel intensity on average as the surface temperature decays over the layer. This intensity decay is greater than those printed in the second or third melt order due to the time between melt one and the captured image. The ability of NIR to determine thermal signatures and predict mechanical properties is not currently present. Another useful analysis performed with NIR images is the ability to detect and visualize internal porosity using automatically exposed images. Figure 29a is a reconstruction porosity from samples 2-L7 and 2-F11. This reconstruction reveals a clear trend of porosity banding. This banding occurs when printing only the twenty tensile bars and not the fixtures and the tensile bars. While Figure 29a only shows two of the printed bars for clarity, the porosity distribution spans all printed tensile bars. By measuring the distance from the bottom of the failed samples to the fracture surface, 9 of the 11 tested samples failed in a banded region of higher porosity, as seen in Figure 29b. The size of NIR detected porosity is limited to greater than 100 μm by the camera resolution. Investigation of two fracture surfaces from Figure 29a shows pores ranging from 20 μm to 300 μm in diameter, as seen in Figure 30.

The porosity formation across the tensile bars increases dramatically when the fixtures are not being melted and the layer time is shorter. This results in bands of porosity appearing in five different regions, where if not healed by subsequent melting, these pore bands are likely sites for failure during mechanical testing. This analysis indicates that the layer time is low which initiates little to no post heat. This lack of post heat compared to layers printed with the fixtures creates insufficient energy likely

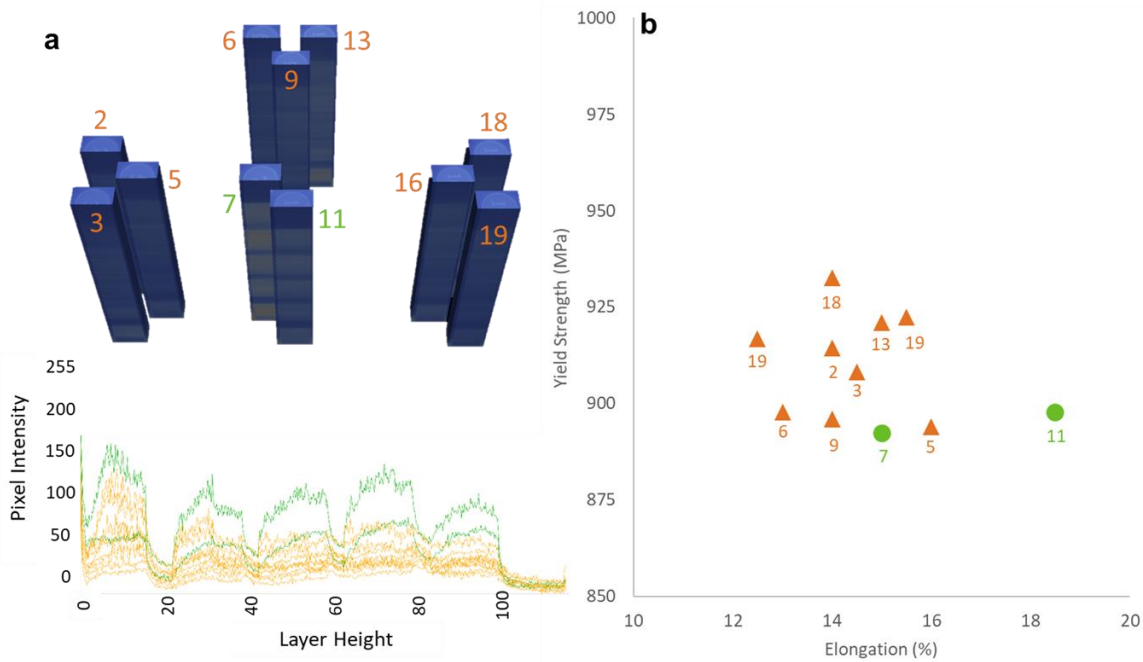

Figure 28: (a) NIR Pixel Intensity visual and plot of samples from B2 tracked for every layer. Green signifies parts printed in the center of the build plate with expected low yield strength while orange signifies parts printed on the edges of the build plate with expected higher yield strength. (b) Yield strength versus elongation of samples from B2 where center (green circle) and edge (orange triangle) parts from (a)

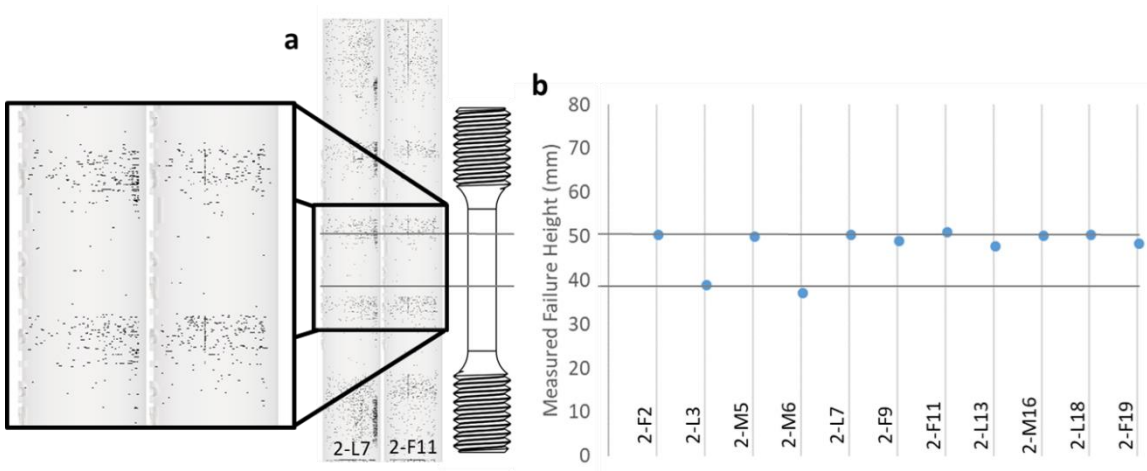

Figure 29: (a) NIR detected porosity in Samples 2-L7 & 2-F11 (b) Failure height measurements from samples tested in B2

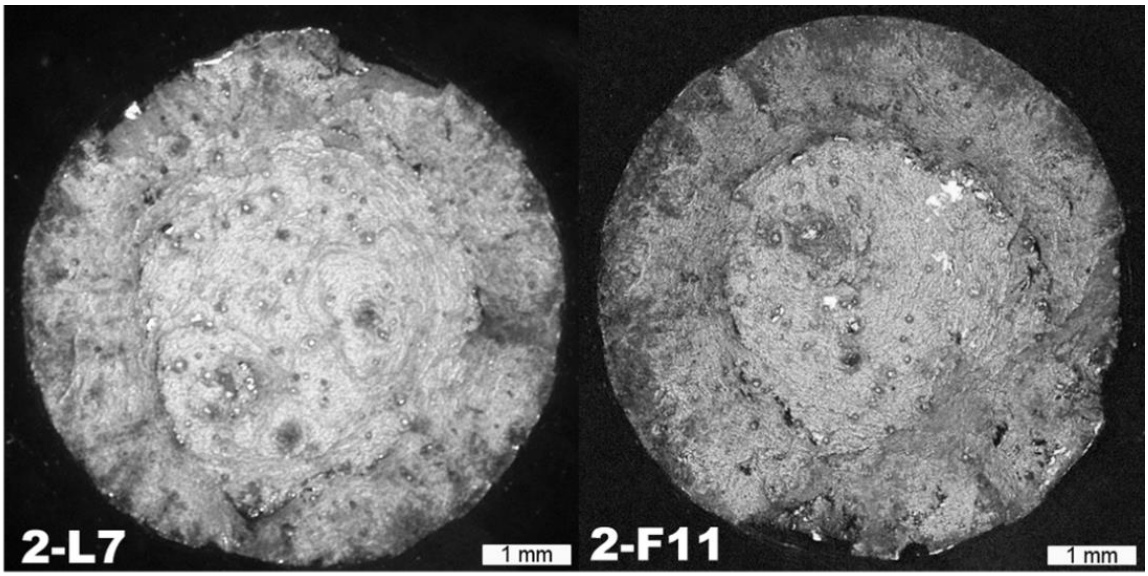

Figure 30: Fracture surfaces of Samples 2-L7 & 2-F11

causing lack of fusion defects. For these reasons when designing a build, it is important to account for the entire build geometry, not just the parts of interest, as a processing variable to track where dramatic changes in layer cross section influence the porosity formation.

After establishing that the cross-sectional area of the entire build chamber influences porosity formation, untested Sample 2-L14 was sectioned and mounted for optical microscopy and hardness testing to determine if the microstructure was affected in a similar manner. Untested 2L-14 was selected as a prime candidate for comparing the microstructure to 2-L7 due to similar location and identical melt order. The region of interest overlapped an area where porosity was detected in NIR images and the fixtures started printing again after being off. Figure 31a shows a stitched optical image of the

etched region of interest for Sample 2-L14 that covers the banding in porosity. Investigation of this region confirms our previous conclusion that lack of fusion defects are concentrated in the banded region.

No noticeable changes are present in the optical imaging; therefore, hardness indentation was performed on this region to see if plastic deformation changes over the region. Figure 31b indicates the location in the X-Z plane and the results of hardness indentation measurements for a jet color map from 300 to 360 Hv. The average hardness of the sample is 338 ± 8.44 Hv, which is lower than reported in literature by Hrabe and Quinn and by Kasperovish and Hausmann [36] [37]. However, the expected yield strength of this material should compare with Sample 2-L7 (894 MPa) which indicates lower than reported hardness values are due to coarser microstructure. This hardness map shows that microstructural variation from top to bottom fluctuates between 335 to 355 Hv. It was hypothesized that a clear band of hardness shift would form similar to the porosity formation where the build cross-sectional area changes. This is not the case likely due to the thermal cycling of the material as subsequent layers are melted. Therefore, the microstructural evolution occurs uniformly related to the cooling curve of the material.

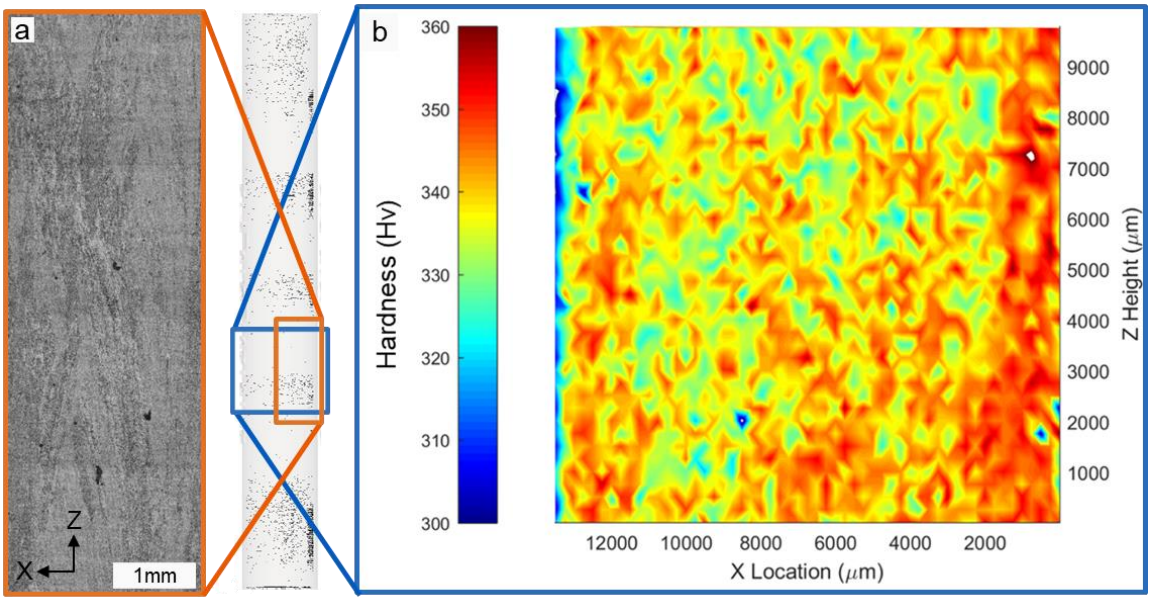

Figure 31: (a) Etched micrograph in X-Z plane of Untested Sample 2-L14. (b) Vickers Hardness test across etched region shown in (a)

CHAPTER FIVE

CONCLUSIONS AND FUTURE WORK

This study has found results relevant to the certification and qualification of the Arcam E-PBF process. Some commonly modified process parameters were mapped to determine if the changes observed in literature can be attributed to the changes made in their study. These results prove that no other changes are made in the machine intent conditions when altering the speed function such that confidence in the results is restored. However, those looking to optimize build times by removing or reducing contours passes must be aware of the change in cooling curve from post heating/cooling which can influence the microstructure over the course of a build. While this study provided a limited scope for the process parameters, a full understanding of the log file parameters will allow the research community to make smarter decisions related to changes in process variables. This will help to provide a more fundamental understanding of the process as it relates to changes in the processing variables and correlations to the process-microstructure space will be more easily explained.

The preliminary investigation of the surface temperature appears to be useful in controlling microstructure. However, further exploration is needed to determine the limitations of surface temperature. Questions such as is this process limited to only z-height sections or can it be used on a part to part basis. While this study has shown the usefulness of the surface temperature variable on the ability to control as-fabricated microstructure, it is imperative to test the samples in uniaxial tension such that bulk material properties can be determined.

For Part 2, this work has shown the importance of understanding the impact of modifying build setup on samples in the as-fabricated condition. The exploration of the overlooked in-situ data collected was completed and correlated to bulk mechanical properties for three extrinsic variables: melt order, build volume, and cross-sectional area. Significant impacts on mechanical performance from increasing build volume and decreasing melt area per layer appeared in this study. However, the order in which parts are melted effects only the correlation for NIR intensity to mechanical strength, but not the yield strength of the material. The defect formation is highly influenced by cross sectional area, but microstructure evolution appears to not. Image and log file data analysis discussed in this study, along with modeling and simulation, is vital to understanding mechanical performance and rationalizing results from the AM technology in a way conventional manufacturing simply cannot achieve. These results show a need to qualify parts using methods other than qualification and certification bars found in traditional methods. Each bar may contain very different thermal signatures and pore structure as compared to the parts of interest which makes traditional qualification metrics difficult to rationalize with test coupons.

Future work for the contents of this work include the determination of all build setup variables that may play a role in the as-fabricated defect- and micro-structure. This investigation will provide design-based guidelines for users to start from a consistent and repeatable baseline. Along with design guidelines, it is possible to relate secondary dendrite arm spacing with effective cooling curve [15]. With this information, it is be possible to determine the cooling curve based on as-fabricated microstructure for each of

the samples tested. This information can be used to recreate the time temperature curve for each as-fabricated sample such that modeling efforts can be fit to match the results.

Finally, in terms of the quantification tools developed, it is necessary to determine the effectiveness of resolving as-fabricated porosity. This would require using other evaluation techniques such as x-ray chromatography or serial sectioning of samples to determine what percentage of porosity is retained through subsequent layers. This will provide a reliability factor of the NIR characterization such that it can stand alone as a form of non-destructive evaluation.

By completing these tasks in the future, the goal of process controlled and in-situ certified components may be realized. As research pushes away from microstructural interactions in well characterized material systems towards machine certification and qualification metrics, studies like this will become more prevalent. The goal to know within a certain confidence level what the microstructure and defect structure is in an as-fabricated part is within reach as studies like this strive to make additive manufacturing a commercially viable option.

LIST OF REFERENCES

[1] ASTM, “Standard Terminology for Additive Manufacturing Technologies,” *ASTM Stand.*, pp. 2–4, 2013.
[2] Arcam AB, “Q Series Manual.” Arcam AB, Mölndal, Sweden, 2014.
[3] W. J. Sames, “Additive manufacturing of inconel 718 using electron beam melting: processing, post-processing, & mechanical properties,” no. May 2015, p. 339, 2015.
[4] I. Gibson, D. W. D. W. Rosen, and B. Stucker, *Additive Manufacturing Technologies: Rapid Prototyping to Direct Digital Manufacturing*, vol. 54. 2009.
[5] Arcam AB, “Private Communication with Arcam AB.” 2018.
[6] W. E. Frazier, “Metal additive manufacturing: A review,” *J. Mater. Eng. Perform.*, vol. 23, no. 6, pp. 1917–1928, 2014.
[7] N. Hrabe and T. Quinn, “Effects of processing on microstructure and mechanical properties of a titanium alloy (Ti-6Al-4V) fabricated using electron beam melting (EBM), Part 2: Energy input, orientation, and location,” *Mater. Sci. Eng. A*, vol. 573, pp. 271–277, 2013.
[8] C. A. Steed, W. Halsey, R. Dehoff, S. L. Yoder, V. Paquit, and S. Powers, “Falcon: Visual analysis of large, irregularly sampled, and multivariate time series data in additive manufacturing,” *Comput. Graph.*, vol. 63, pp. 50–64, 2017.
[9] C. A. Steed *et al.*, “Big data visual analytics for exploratory earth system simulation analysis,” *Comput. Geosci.*, vol. 61, pp. 71–82, 2013.
[10] G. Lütjering and J. Williams, *Titanium*, 2nd ed. Berlin, Heidelberg: Springer Berlin Heidelberg, 2007.
[11] T. Ahmed and H. J. Rack, “Phase transformations during cooling in α+β titanium alloys,” *Mater. Sci. Eng. A*, vol. 243, no. 1–2, pp. 206–211, 1998.
[12] R. W. Armstrong, “Engineering science aspects of the Hall – Petch relation,” vol. 1028, no. February, pp. 1013–1028, 2014.
[13] X. Tan *et al.*, “Graded microstructure and mechanical properties of additive manufactured Ti-6Al-4V via electron beam melting,” *Acta Mater.*, vol. 97, pp. 1–16, 2015.
[14] N. Hrabe, T. Gnupel-Herold, and T. Quinn, “Fatigue properties of a titanium alloy (Ti-6Al-4V) fabricated via electron beam melting (EBM): Effects of internal defects and residual stress,” *Int. J. Fatigue*, vol. 94, pp. 202–210, 2015.
[15] S. S. Al-Bermani, M. L. Blackmore, W. Zhang, and I. Todd, “The origin of microstructural diversity, texture, and mechanical properties in electron beam melted Ti-6Al-4V,” *Metall. Mater. Trans. A Phys. Metall. Mater. Sci.*, vol. 41, no. 13, pp. 3422–3434, 2010.
[16] P. Edwards, A. O’Conner, and M. Ramulu, “Electron Beam Additive Manufacturing of Titanium Components: Properties and Performance,” *J. Manuf. Sci. Eng.*, vol. 135, no. 6, p. 061016, 2013.
[17] H. Galarraga, D. A. Lados, R. R. Dehoff, M. M. Kirka, and P. Nandwana, “Effects of the microstructure and porosity on properties of Ti-6Al-4V ELI alloy fabricated by electron beam melting (EBM),” *Addit. Manuf.*, vol. 10, pp. 47–57, 2016.
[18] S. M. Kelly and S. L. Kampe, “Microstructural evolution in laser-deposited multilayer Ti-6Al-4V builds: Part II. Thermal modeling,” *Metall. Mater. Trans. A*,

vol. 35, no. 6, pp. 1861–1867, 2004.
[19] M. Seifi, A. Salem, D. Satko, J. Shaffer, and J. J. Lewandowski, "Defect distribution and microstructure heterogeneity effects on fracture resistance and fatigue behavior of EBM Ti-6Al-4V," *Int. J. Fatigue*, vol. 94, pp. 263–287, 2017.
[20] D. Rosenthal, "The Theory of Moving Sources of Heat and Its Application of Metal Treatments," *Trans. ASME*, vol. 68, pp. 849–866, 1946.
[21] A. A. Antonysamy, J. Meyer, and P. B. Prangnell, "Effect of build geometry on the Beta-grain structure and texture in additive manufacture of Ti6Al4V by selective electron beam melting," *Mater. Charact.*, vol. 84, pp. 153–168, 2013.
[22] Z. C. Cordero, R. B. Dinwiddie, D. Immel, and R. R. Dehoff, "Nucleation and growth of chimney pores during electron-beam additive manufacturing," *J. Mater. Sci.*, vol. 52, no. 6, pp. 3429–3435, 2017.
[23] R. R. Dehoff *et al.*, "Site specific control of crystallographic grain orientation through electron beam additive manufacturing," *Mater. Sci. Technol.*, vol. 31, no. 8, pp. 931–938, 2015.
[24] H. Gong, K. Rafi, H. Gu, G. D. Janaki Ram, T. Starr, and B. Stucker, "Influence of defects on mechanical properties of Ti-6Al-4V components produced by selective laser melting and electron beam melting," *Mater. Des.*, vol. 86, pp. 545–554, 2015.
[25] H. Gong, H. K. Rafi, N. V Karthik, T. Starr, and B. Stucker, "Defect Morphology of Ti-6Al-4V Parts Fabricated by Selective Laser and Electron Beam Melting," *J. Mater. Eng. Perform.*, vol. 22, no. 12, pp. 3872–3883, 2013.
[26] C. Guo, W. Ge, and F. Lin, "Effects of scanning parameters on material deposition during Electron Beam Selective Melting of Ti-6Al-4V powder," *J. Mater. Process. Technol.*, vol. 217, pp. 148–157, 2015.
[27] W. J. Sames, F. A. List, S. Pannala, R. R. Dehoff, and S. S. Babu, "The metallurgy and processing science of metal additive manufacturing," *Int. Mater. Rev.*, vol. 6608, no. March, pp. 1–46, 2016.
[28] L. E. Murr, "Metallurgy of additive manufacturing: Examples from electron beam melting," *Addit. Manuf.*, vol. 5, pp. 40–53, 2015.
[29] S. P. Narra, R. Cunningham, J. Beuth, and A. D. Rollett, "Location specific solidification microstructure control in electron beam melting of Ti-6Al-4V," *Addit. Manuf.*, vol. 19, pp. 160–166, 2018.
[30] M. Seifi, D. Christiansen, J. L. Beuth, O. Harrysson, and J. J. Lewandowski, "Process Mapping, Fracture and Fatigue Behavior of Ti-6Al-4V Produced by EBM Additive Manufacturing," *Proc. 13th World Conf. Titan.*, no. August, pp. 1373–1377, 2016.
[31] P. Nandwana, M. M. Kirka, V. C. Paquit, S. Yoder, and R. R. Dehoff, "Correlations Between Powder Feedstock Quality, In Situ Porosity Detection, and Fatigue Behavior of Ti-6Al-4V Fabricated by Powder Bed Electron Beam Melting: A Step Towards Qualification," *Jom*, vol. 70, no. 9, pp. 1686–1691, 2018.
[32] N. Meisel and C. Williams, "An Investigation of Key Design for Additive Manufacturing Constraints in Multimaterial Three-Dimensional Printing," *J. Mech. Des.*, vol. 137, no. 11, p. 111406, 2015.
[33] S. M. Kelly and S. L. Kampe, "Microstructural evolution in Laser-Deposited

multilayer Ti6Al-4V build: Part I. Microstructural characterization," *Metall. Mater. Trans. A*, vol. 35, no. June, pp. 1861–1867, 2004.

[34] ASTM, "Standard Test Method for Knoop and Vickers Hardness of Materials," *ASTM Stand.*, pp. 1–43, 2016.

[35] ASTM, "Standard Test Methods for Tension Testing of Metallic Materials," *ASTM Stand.*, no. C, pp. 1–27, 2016.

[36] N. Hrabe and T. Quinn, "Effects of processing on microstructure and mechanical properties of a titanium alloy (Ti-6Al-4V) fabricated using electron beam melting (EBM), part 1: Distance from build plate and part size," *Mater. Sci. Eng. A*, vol. 573, pp. 264–270, 2013.

[37] G. Kasperovich and J. Hausmann, "Improvement of fatigue resistance and ductility of TiAl6V4 processed by selective laser melting," *J. Mater. Process. Technol.*, vol. 220, pp. 202–214, 2015.

APPENDIX

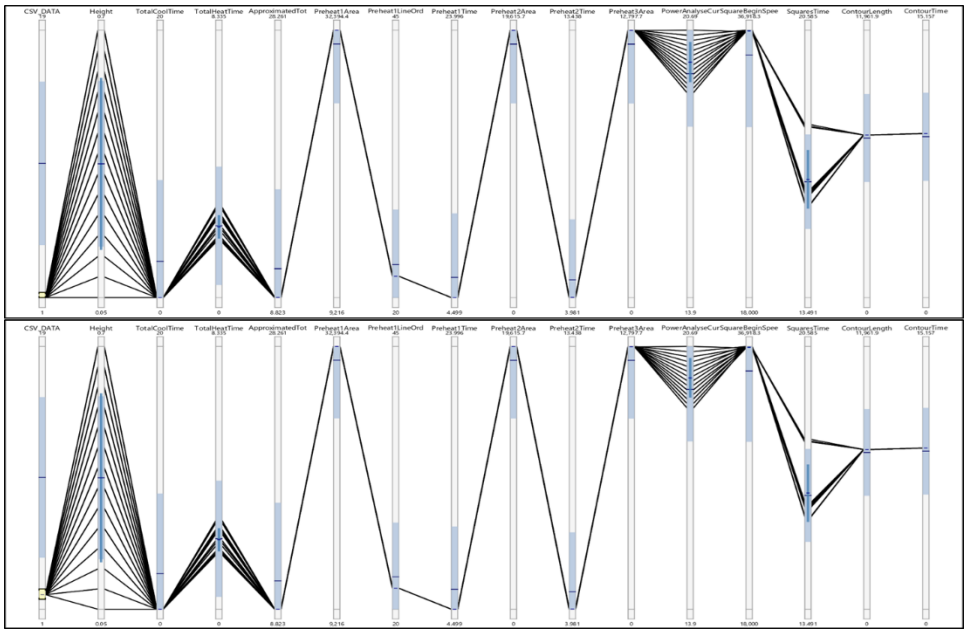

Comparison of Set 1: Standard Melt Theme (Top) and Set 2: Post Heat Max 20s to 10s (Bottom)

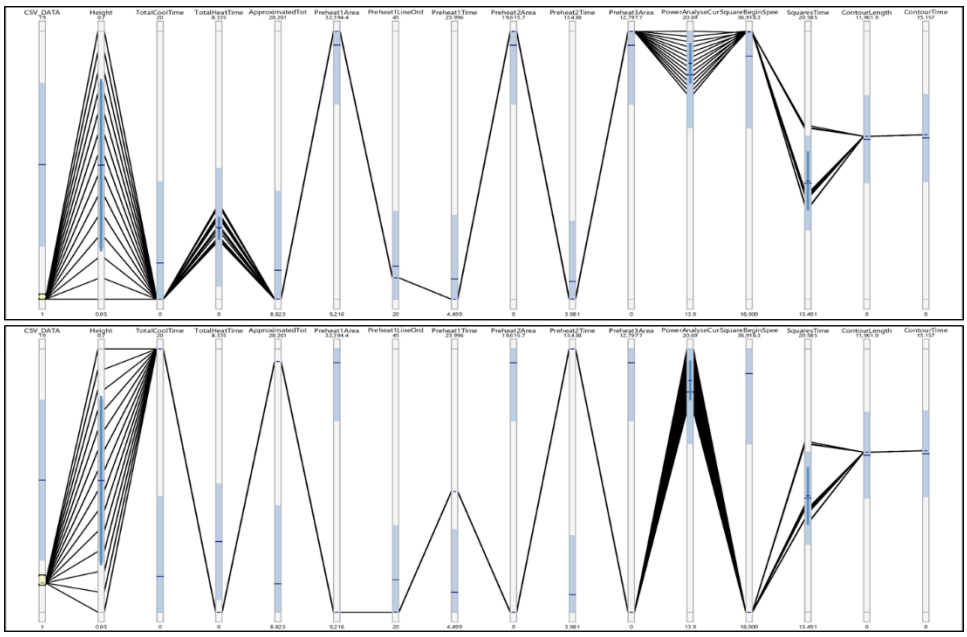

Comparison of Set 1: Standard Melt Theme (Top) and Set 3: Preheat Square Auto Box Calc True to False (Bottom)

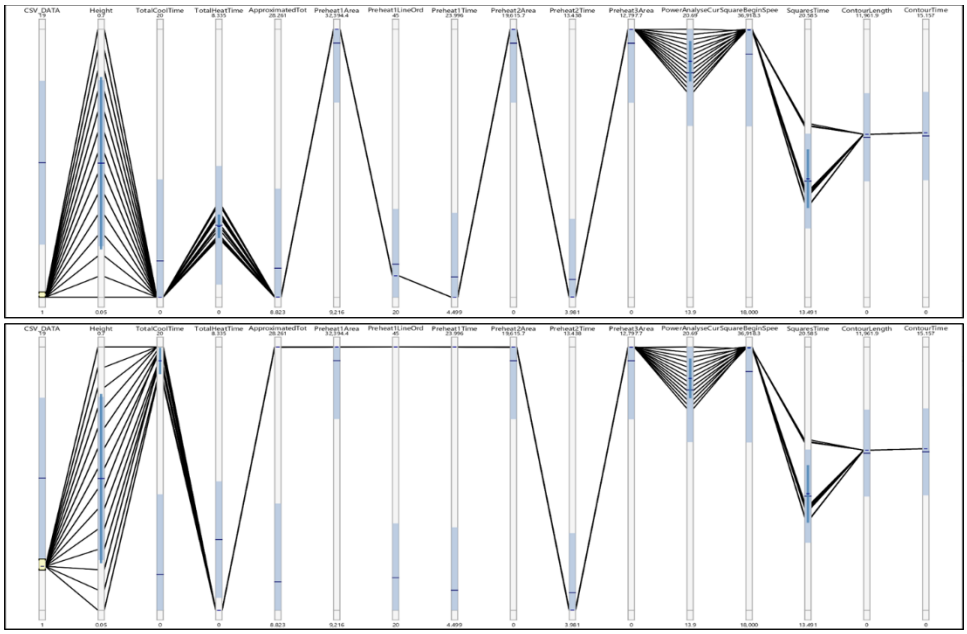

Comparison of Set 1: Standard Melt Theme (Top) and Set 4: Preheat I Max Beam Current 16 to 32mA (Bottom)

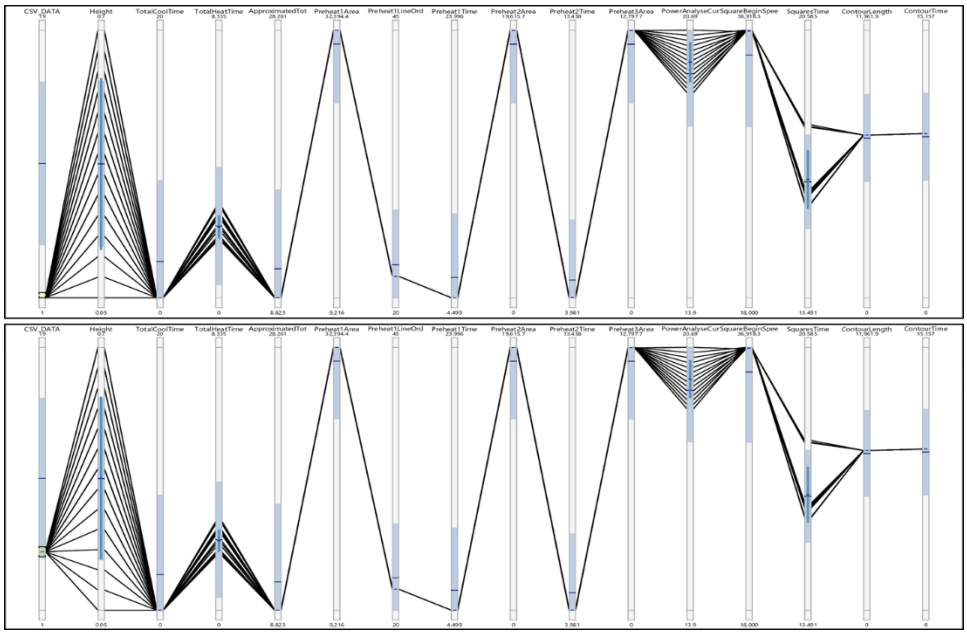

Comparison of Set 1: Standard Melt Theme (Top) and Set 5: Preheat I Max # of Reps 20 to 40 (Bottom)

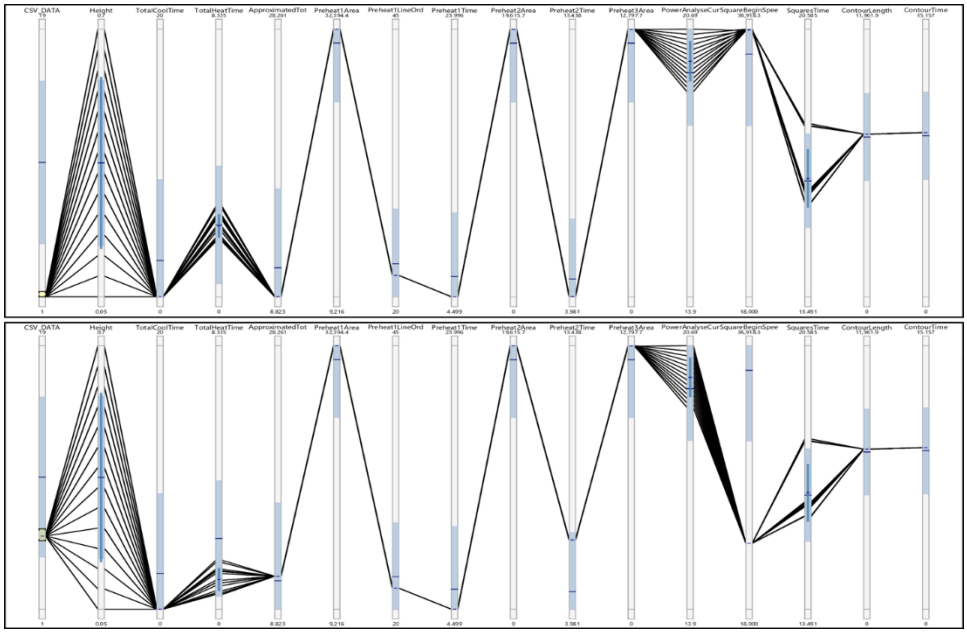

Comparison of Set 1: Standard Melt Theme (Top) and Set 6: Preheat II Max Beam Current 19 to 38mA (Bottom)

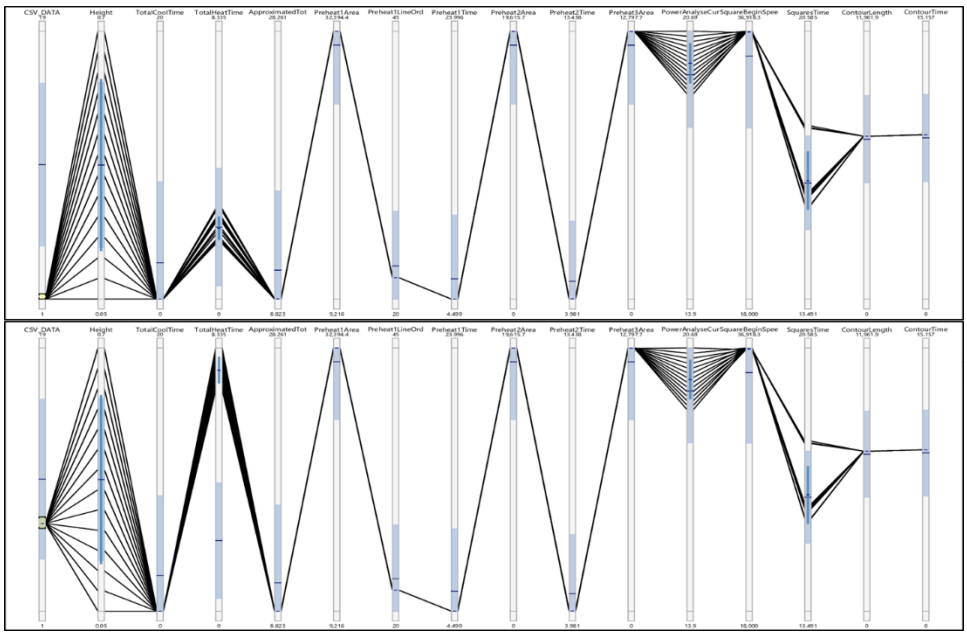

Comparison of Set 1: Standard Melt Theme (Top) and Set 7: Preheat II Avg Current 5.4 to 8.0mA (Bottom)

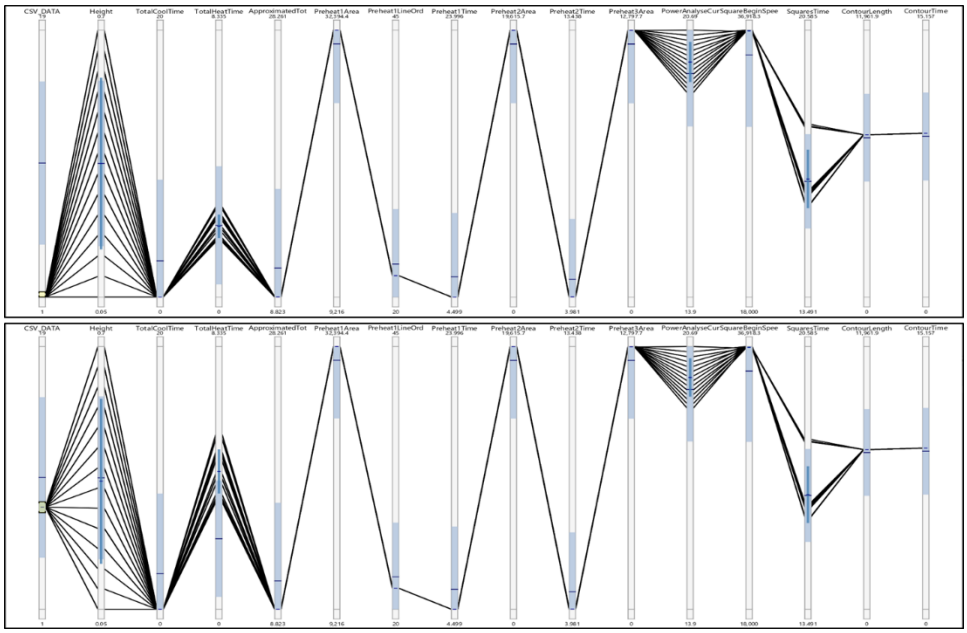

Comparison of Set 1: Standard Melt Theme (Top) and Set 8: Preheat Heater 2 Current 48 to 30mA (Bottom)

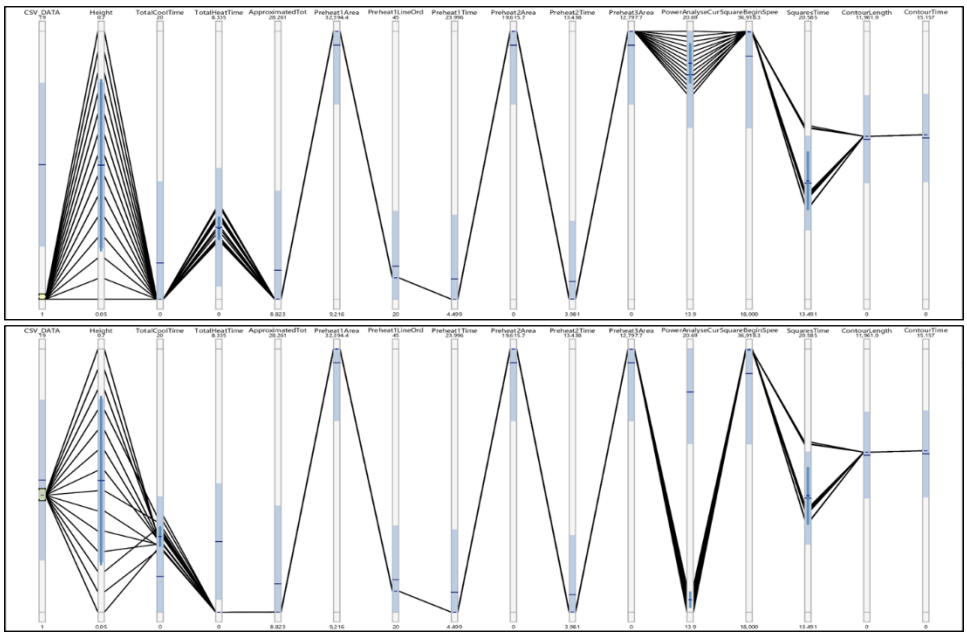

Comparison of Set 1: Standard Melt Theme (Top) and Set 9: Melt Power Temp 940 to 840 (Bottom)

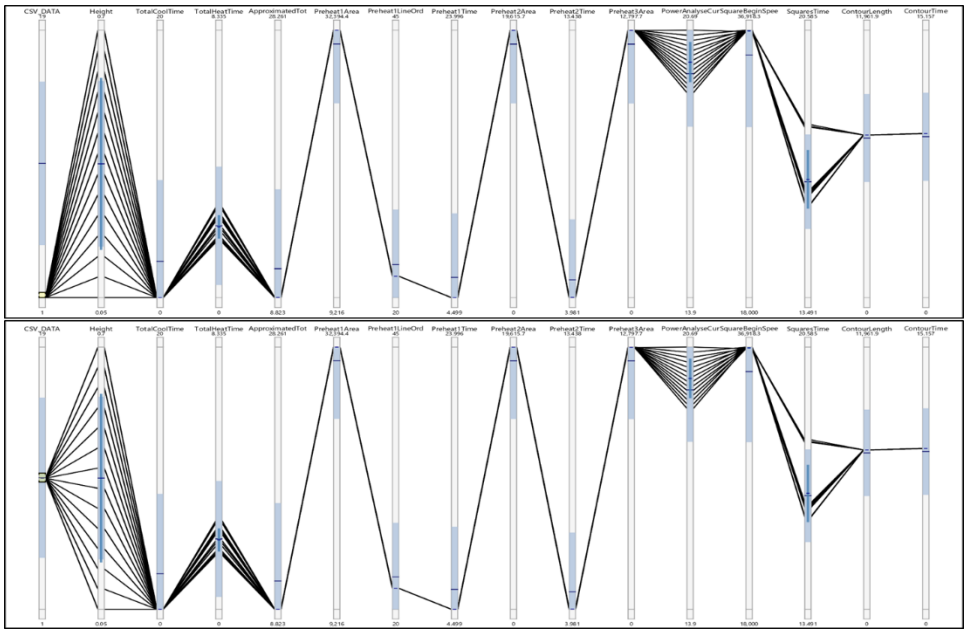

Comparison of Set 1: Standard Melt Theme (Top) and Set 10: Melt Power Min Current 3 to 10mA (Bottom)

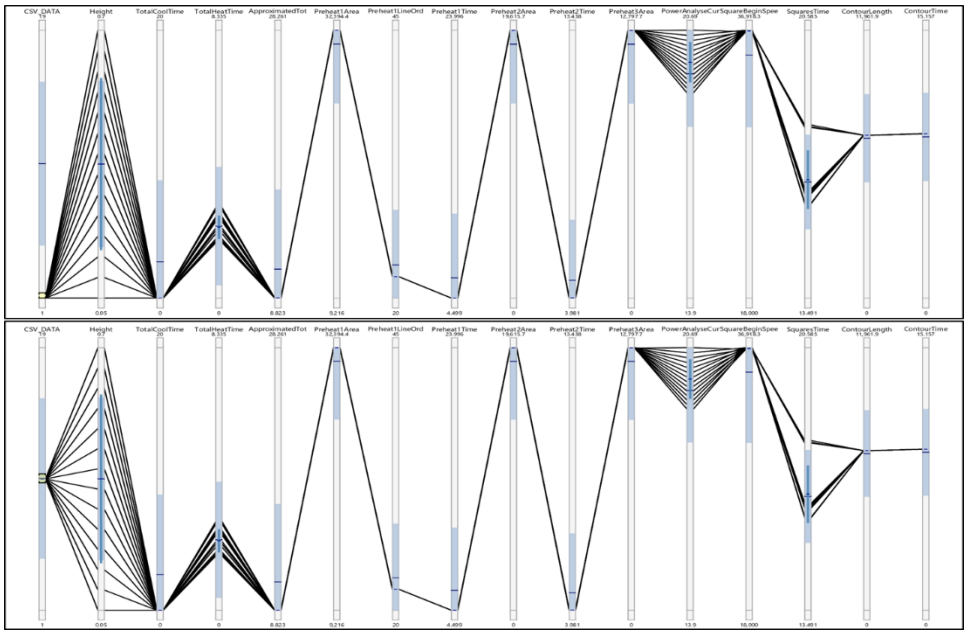

Comparison of Set 1: Standard Melt Theme (Top) and Set 11: Melt Contour # 3 to 5 (Bottom)

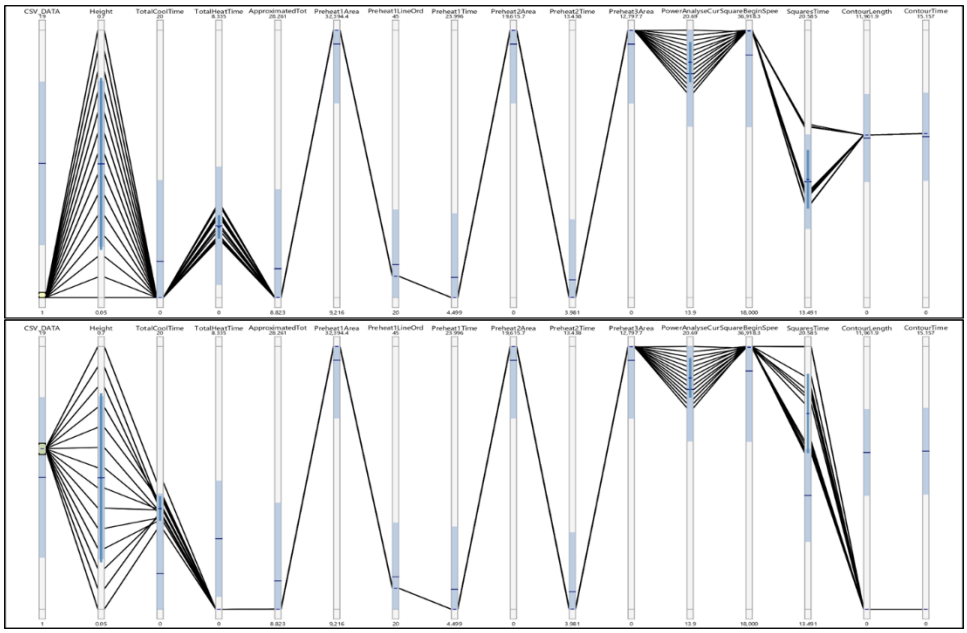

Comparison of Set 1: Standard Melt Theme (Top) and Set 12: Melt Contour # 3 to 0 (Bottom)

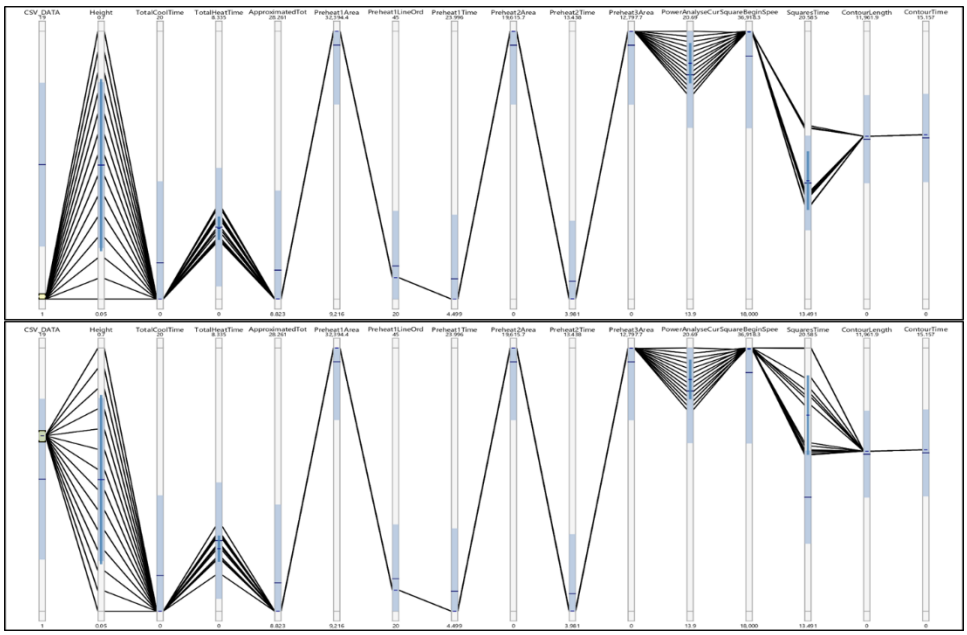

Comparison of Set 1: Standard Melt Theme (Top) and Set 13: Melt Hatch offset to contour 0 to -1mm (Bottom)

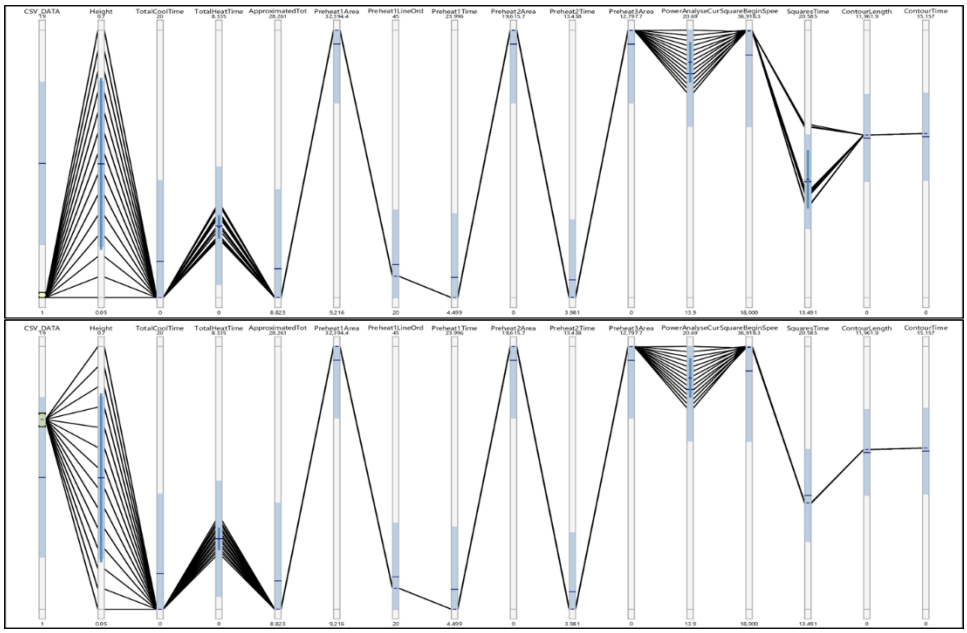

Comparison of Set 1: Standard Melt Theme (Top) and Set 14: Melt Hatch Use Rotating Hatch True to False (Bottom)

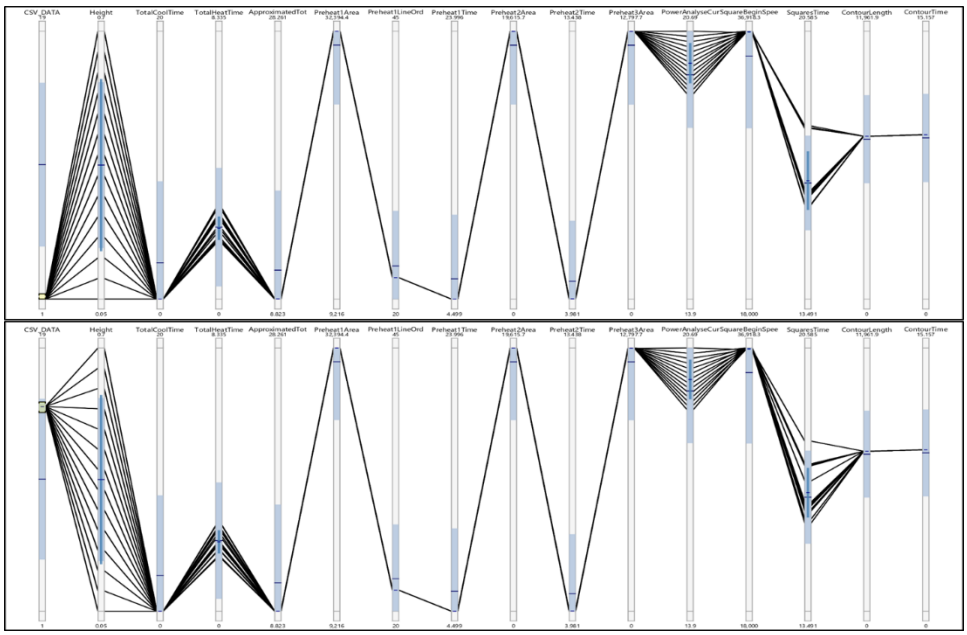

Comparison of Set 1: Standard Melt Theme (Top) and Set 15: Melt Hatch Square Rotating Angle per MM 1350 to 750 (Bottom)

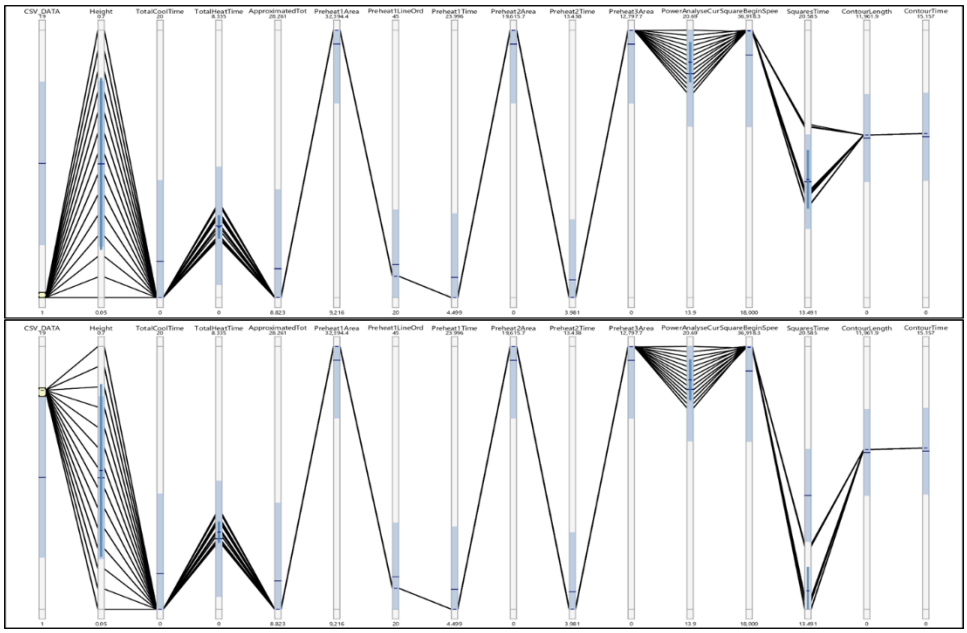

Comparison of Set 1: Standard Melt Theme (Top) and Set 16: Melt Beam Speed Function 60 to 72 (Bottom)

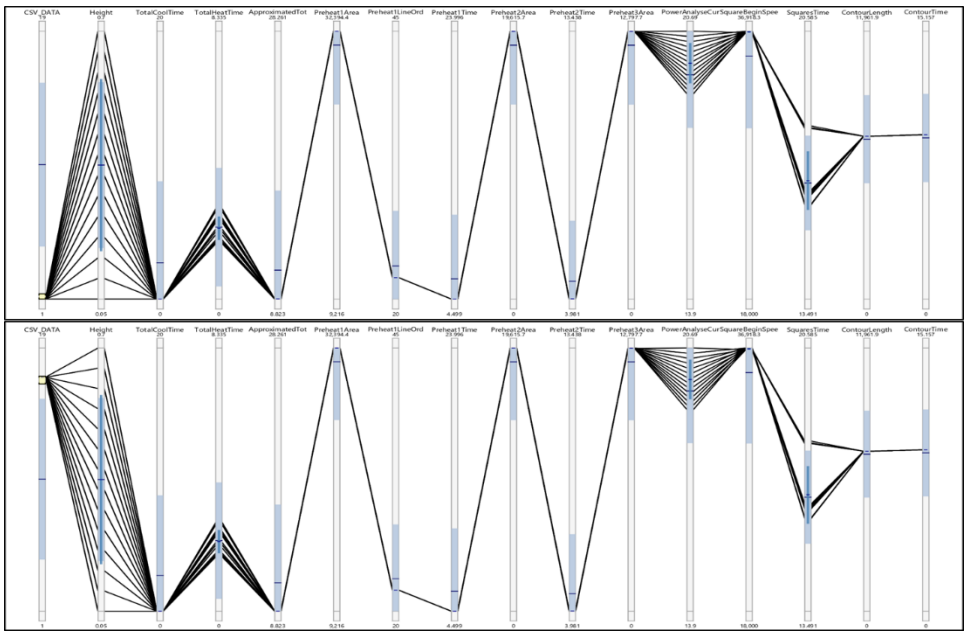

Comparison of Set 1: Standard Melt Theme (Top) and Set 17: Melt Beam Focus Offset 36 to 24 (Bottom)

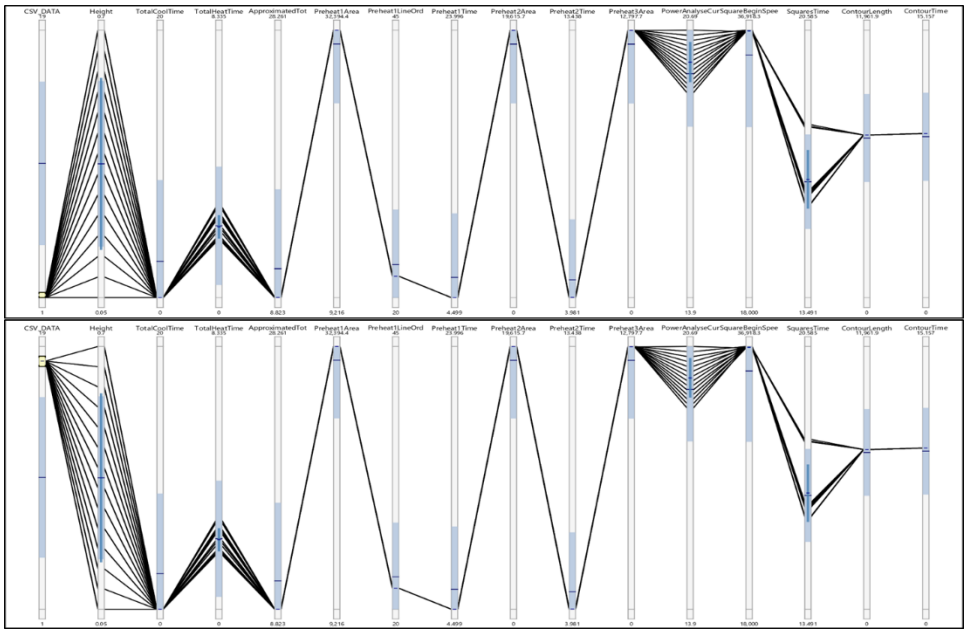

Comparison of Set 1: Standard Melt Theme (Top) and Set 18: Melt Hatch Square Thickness True to False (Bottom)

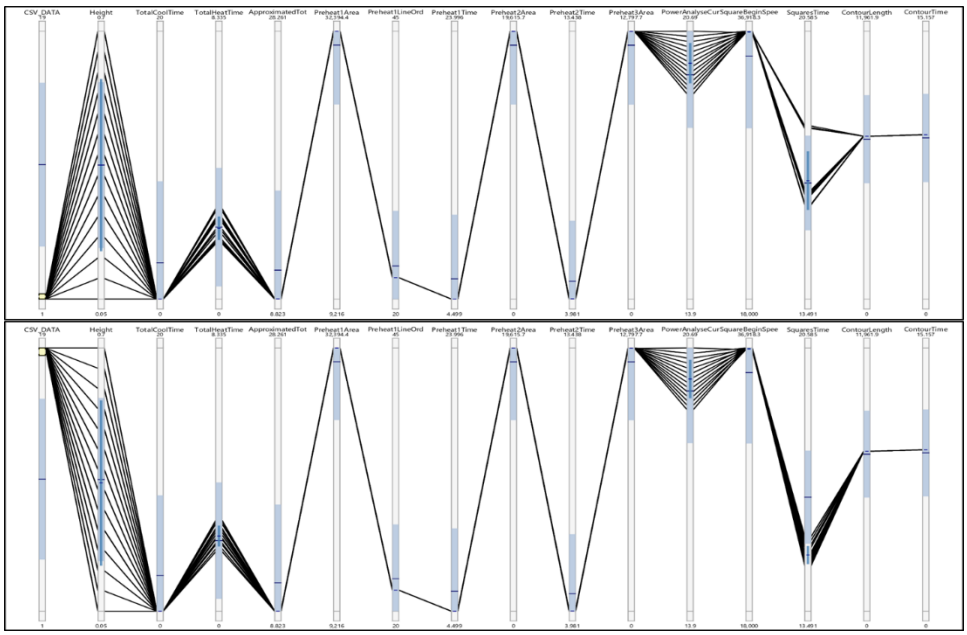

Comparison of Set 1: Standard Melt Theme (Top) and Set 19: Melt Optimise Optimal Hatch Length 62 to 75mm (Bottom)

VITA

Sean L. Yoder was born in Knoxville, TN and graduated from Bearden HS in May 2011. From there, his search of knowledge took him Maryville College to play four years of varsity soccer for the Scots. Sean was able to acquire a bachelor's degree in science. He successfully bridged the gap between Maryville and the University of Tennessee – Knoxville to complete his second undergraduate degree in Mechanical Engineering. His final year of undergraduate landed him a post-bachelor position at the ORNL Manufacturing Demonstration Facility to support research in metal Additive Manufacturing. He gained confidence and knowledge in his abilities so much that he decided to go back to school to pursue a Master's degree in Mechanical Engineering focuses on AM technology. Sean has published one first author publication relating AM to topology optimization and provided support for three other publications in the AM community. His final contribution for his graduate work is to submit work published in this thesis to the AM community to spread his knowledge of the process. Sean hopes to use the skills he has learned to further a career in the AM space by applying the process to fabricate components. This is the beginning of his professional career in the engineering community.